

This is an Open Access document downloaded from ORCA, Cardiff University's institutional repository:<https://orca.cardiff.ac.uk/id/eprint/162041/>

This is the author's version of a work that was submitted to / accepted for publication.

Citation for final published version:

Queiroz de Azevedo, Allana, Jiménez-Espejo, Francisco J., Bulian, Francesca, Sierra, Francisco J., Tanguan, Deborah, Takashimizu, Yasuhiro, Albuquerque, Ana Luiza S., Kubota, Kaoru, Escutia, Carlota, Norris, Richard D., Hemming, Sidney R. and Hall, Ian R. 2023. Orbital forcing and evolution of the Southern African Monsoon from late Miocene to early Pliocene. *Paleoceanography and Paleoclimatology* 38 (9) , e2022PA004588. 10.1029/2022PA004588

Publishers page: <http://dx.doi.org/10.1029/2022PA004588>

Please note:

Changes made as a result of publishing processes such as copy-editing, formatting and page numbers may not be reflected in this version. For the definitive version of this publication, please refer to the published source. You are advised to consult the publisher's version if you wish to cite this paper.

This version is being made available in accordance with publisher policies. See <http://orca.cf.ac.uk/policies.html> for usage policies. Copyright and moral rights for publications made available in ORCA are retained by the copyright holders.



Paleoceanography and Paleoclimatology



RESEARCH ARTICLE

10.1029/2022PA004588

Key Points:

- From 7.4 to 4.5 Ma, the Southern African Monsoon (SAFM) was driven by precession and the long eccentricity cycles related to internal feedbacks
- Weak Northern African monsoon was coeval with intense SAFM during the acme of the Messinian Salinity Crisis
- The SAFM intensity and *Orbulina universa* responded to changes in the Antarctic ice sheet during the latest Miocene

Correspondence to:

F. J. Jiménez-Espejo,
francisco.jimenez@csic.es

Citation:

de Azevedo, A. Q., Jiménez-Espejo, F. J., Bulian, F., Sierro, F. J., Tanguan, D., Takashimizu, Y., et al. (2023). Orbital forcing and evolution of the Southern African Monsoon from late Miocene to early Pliocene. *Paleoceanography and Paleoclimatology*, 38, e2022PA004588. <https://doi.org/10.1029/2022PA004588>

Received 1 DEC 2022
Accepted 14 JUL 2023

Author Contributions:

Conceptualization: Allana Queiroz de Azevedo, Francisco J. Jiménez-Espejo, Francesca Bulian, Francisco J. Sierro, Deborah Tanguan

Formal analysis: Allana Queiroz de Azevedo, Francisco J. Jiménez-Espejo, Francesca Bulian, Francisco J. Sierro, Yasuhiro Takashimizu, Kaoru Kubota









Funding acquisition: Francisco J. Jiménez-Espejo, Ana Luiza S. Albuquerque, Carlota Escutia

Investigation: Allana Queiroz de Azevedo, Francisco J. Jiménez-Espejo, Francisco J. Sierro, Yasuhiro Takashimizu, Kaoru Kubota, Carlota Escutia

© 2023. The Authors.

This is an open access article under the terms of the [Creative Commons Attribution-NonCommercial-NoDerivs License](#), which permits use and distribution in any medium, provided the original work is properly cited, the use is non-commercial and no modifications or adaptations are made.

Orbital Forcing and Evolution of the Southern African Monsoon From Late Miocene to Early Pliocene

Allana Queiroz de Azevedo¹ , Francisco J. Jiménez-Espejo^{2,3} , Francesca Bulian^{4,5}, Francisco J. Sierro⁴ , Deborah Tanguan⁶, Yasuhiro Takashimizu⁷ , Ana Luiza S. Albuquerque¹ , Kaoru Kubota³ , Carlota Escutia², Richard D. Norris⁸ , Sidney R. Hemming⁹, and Ian R. Hall⁶ 

¹Programa de Pós-Graduação em Geoquímica, Universidade Federal Fluminense, Rio de Janeiro, Brazil, ²Instituto Andaluz de Ciencias de la Tierra, Consejo Superior de Investigaciones Científicas-Universidad de Granada, Armilla, Spain, ³Japan Agency for Marine–Earth Science and Technology (JAMSTEC), Yokosuka, Japan, ⁴Department of Geology, Universidad de Salamanca, Salamanca, Spain, ⁵Groningen Institute of Archeology, University of Groningen, Groningen, The Netherlands, ⁶School of Earth and Environmental Sciences, Cardiff University, Cardiff, UK, ⁷Mathematical and Natural Sciences, Niigata University, Niigata, Japan, ⁸Scripps Institution of Oceanography, University of California San Diego, San Diego, CA, USA, ⁹Department of Earth and Environmental Sciences, Lamont-Doherty Earth Observatory, New York, NY, USA

Abstract The late Miocene-early Pliocene (7.4–4.5 Ma) is a key interval in Earth's history where intense reorganization of atmospheric and ocean circulation occurred within a global cooling scenario. The Southern African monsoon (SAFM) potentially played an important role in climate systems variability during this interval. However, the dynamics of this important atmospheric system is poorly understood due to the scarcity of continuous records. Here, we present an exceptional continuous late Miocene to early Pliocene reconstruction of SAFM based on elemental geochemistry (Ca/Ti and Si/K ratios), stable isotope geochemistry ($\delta^{18}\text{O}$ and $\delta^{13}\text{C}$ recorded in the planktonic foraminifera *Orbulina universa*), and marine sediment grain size data from the International Ocean Discovery Program (IODP) Site U1476 located at the entrance of the Mozambique Channel. Spectral characteristics of the Si/K ratio (fluvial input) was used to identify the main orbital forcing controlling SAFM. Precession cycles governed precipitation from 7.4 to ~6.9 Ma and during the early Pliocene. From ~6.9 to ~5.9 Ma, the precession and long eccentricity cycles drove the SAFM. The major Antarctic ice sheet expansion across this interval appear to influence the isotopic records of *O. universa* imprinting its long-term variability signal as a response to the ocean and atmospheric reorganization. Precession cycles markedly weakened from 5.9 to 5.3 Ma, almost the same period when the Mediterranean Outflow Water ceased. These findings highlight important teleconnections among the SAFM, Mediterranean Sea, and other tropical regions.

1. Introduction

The Messinian was a time interval that is warmer-than-modern Earth, with $p\text{CO}_2$ levels similar to present day, between 350 and 410 ppm (Steinhilber et al., 2021; Zhang et al., 2013). All future scenarios over the 21st century highlights that global warming will further amplify changes in large-scale atmospheric circulation, increasing the monsoon precipitation and associated flooding, e.g., in Africa (IPCC, 2021).

The late Miocene to early Pliocene (7.4–4.5 Ma) are puzzling epochs within the Neogene, in which intense reorganization of atmospheric circulation took place and led to changes in both hemispheres. Evidence from the South America showed that during this interval the Hadley cell strengthened, enhancing subtropical aridification, and allowing the expansion of C4 vegetation (Carrapa et al., 2019). Such change was accompanied by northward migration of the ITCZ (Allen & Armstrong, 2012) and the westerlies (Allen & Armstrong, 2012; Christensen et al., 2021; Groeneveld et al., 2017; Quan et al., 2014). In northern Africa, tectonic changes and reorganization of atmospheric circulation led to the Northern African Monsoon weakening, the ITCZ decrease its northern range, being more similar to current one, and all this favored the expansion of the Sahara desert (Zhang et al., 2014). In a coeval manner, the southeast Asian winter monsoon intensified (Holbourn et al., 2018; Jöhnck et al., 2020). Moreover, marine gateways configuration also changed during the late Miocene. Betic corridor, Rifian Corridor, and potentially Gibraltar (marine gateways connecting the Atlantic Ocean and the Mediterranean Sea) began to close at that time (Duggen et al., 2003, 2004). Central American Seaway progressively narrowed since 4.8 Ma affecting the AMOC (Bahr et al., 2023).

Methodology: Francisco J. Sierro, Yasuhiro Takashimizu
Project Administration: Francisco J. Jiménez-Espejo, Carlota Escutia
Software: Allana Queiroz de Azevedo
Supervision: Francisco J. Jiménez-Espejo, Francisco J. Sierro, Deborah Tanguan, Ana Luiza S. Albuquerque, Carlota Escutia, Richard D. Norris, Sidney R. Hemming, Ian R. Hall
Validation: Kaoru Kubota
Visualization: Allana Queiroz de Azevedo, Francisco J. Jiménez-Espejo
Writing – original draft: Allana Queiroz de Azevedo, Francisco J. Jiménez-Espejo, Francisco J. Sierro
Writing – review & editing: Allana Queiroz de Azevedo, Francisco J. Jiménez-Espejo, Francesca Bulian, Francisco J. Sierro, Deborah Tanguan, Ana Luiza S. Albuquerque, Kaoru Kubota

The Messinian Salinity Crisis (MSC, 5.95–5.33 Ma, Hsü, 1973; Roveri et al., 2014) is an exceptional event. The marine records in the Mediterranean have been well studied, but atmospheric circulation is poorly known. During the MSC, a complex combination of tectonic activity and/or changes in the glacio-eustatic sea level led to the progressive isolation of the Mediterranean Sea and, once isolated, was very sensitive on the rainfall input. As a result of the MSC, the Mediterranean Outflow Water (MOW) influx into the Atlantic Ocean was severely reduced or ceased (Ng et al., 2022) allowing the formation of a hypersaline deposits (gypsum and halite, salinity >360 g/kg) from ~5.9 to ~5.6 Ma (Roveri et al., 2014). This restriction is suggested to have slowed down the Atlantic Meridional Overturning Circulation (AMOC) by ~15% (Rogerson et al., 2012) as MOW provides considerable amounts of the salinity needed for the formation of North Atlantic Deep Water. During the brackish water phase from ~5.5 to 5.6 Ma (salinity <20 g/kg, Roveri et al., 2014) the climate is thought to return to a bipolar mode, with cooling in the northern hemisphere (caused by an AMOC collapse) and warming in the southern hemisphere (Ivanovic et al., 2014).

Modeling studies suggest the MSC affected sea ice formation in high latitude northern hemisphere (Murphy et al., 2009), with a global salinity reduction of ~6 psu inducing significant sea ice formation (Sun & Liu, 2006) in the Labrador Sea, south of Greenland, and around Iceland (Mudie & Helgason, 1983; Vidal et al., 2002). Moreover, the MSC may have intensified the Southern African Monsoon (SAFM) (Ivanović et al., 2014). These authors showed through projections regarding boundary conditions from the MSC that some physical parameters were affected in the southern hemisphere. Near our study site, occurred positive anomalies of precipitation (~50%), the sea surface temperature (SST) increased (between 1°C and 3°C), and also the surface air temperature showed enhancement (up to 3°C). It was also demonstrated that in regions where surface and intermediate water masses “cooled” the atmosphere overlain these regions also cooled. This occurred close to the Northern African region. From this, the weakening of the Northern African monsoon is associated to mentioned changes, and thus, following the reasoning developed and demonstrated by Ivanovic et al. (2014) one can expect a potential intense SAFM to be observed in the entrance of Mozambique Channel.

Our understanding of the SAFM variability and its reconciliation by teleconnection with other global climate events, i.e., the MSC, is limited due to the scarcity of suitable paleoclimate archives for reconstructions of regional hydroclimate. Modeling predicted that the Mediterranean Sea desiccation took place when northern Africa received abundant rainfall (Griffin, 2002; Marzocchi et al., 2015) likely due strong northern African monsoon in contrast to weak SAFM. However, other modeling data showed that during the acme of MSC the northern Africa experienced a clear warming and received low precipitation (Schneck et al., 2010) due to weak northern African monsoon in comparison to strong SAFM. Despite such efforts to understand the evolution of SAFM and MSC, there is no proxy evidence available at present that reconciles the controversies found by those models. Thus, understanding the dynamic of SAFM and its association with MSC during the Messinian is a great opportunity to shed light on the mechanism behind the changes in atmospheric circulation and precipitation patterns, which may also help constrain accurately future projections of climate change.

Therefore, to unravel this conundrum, we reconstructed the precipitation changes that occurred in the SAFM through elemental geochemistry and $\delta^{18}\text{O}$ of planktonic foraminifera recorded in the International Ocean Discovery Program (IODP) Site U1476 located at the northern entrance of the Mozambique Channel, Indian Ocean. Moreover, to complement our observations from a global perspective of the African monsoon system (northern and southern components) from late Miocene to early Pliocene, we compared in detail our data with the Montemayor-1 borehole located in southwestern Iberia (van der Berg et al., 2015) due its association with the MOW, which is sensitive to monsoonal input by Nile River and also to the MSC. Moreover, the elemental record in Montemayor reflects precession-driven cyclicity in annual rainfall in midlatitude that were considered to be synchronous with meridional shifts in the ITCZ.

2. Study Site

Site U1476 was drilled at the northern entrance of the Mozambique Channel, at Davie Ridge (15°49.25'S; 41°46.12'E), western Indian Ocean (Figure 1) at a water depth of 2,166 m below sea level (mbsf) during the IODP Expedition 361 (Hall et al., 2017). Climatologically, strong air-sea interactions via atmospheric cells (Hadley and Walker) and the surface Mascarene high over the subtropical south Indian Ocean, drive rainfall oscillations in this region (de Oliveira et al., 2018; Kaboth-Bahr et al., 2021; Maslin et al., 2014; Nicholson, 2015). During the austral summer, the ITCZ shifts southward concurrently with the Mascarene high (Xulu et al., 2020) forming

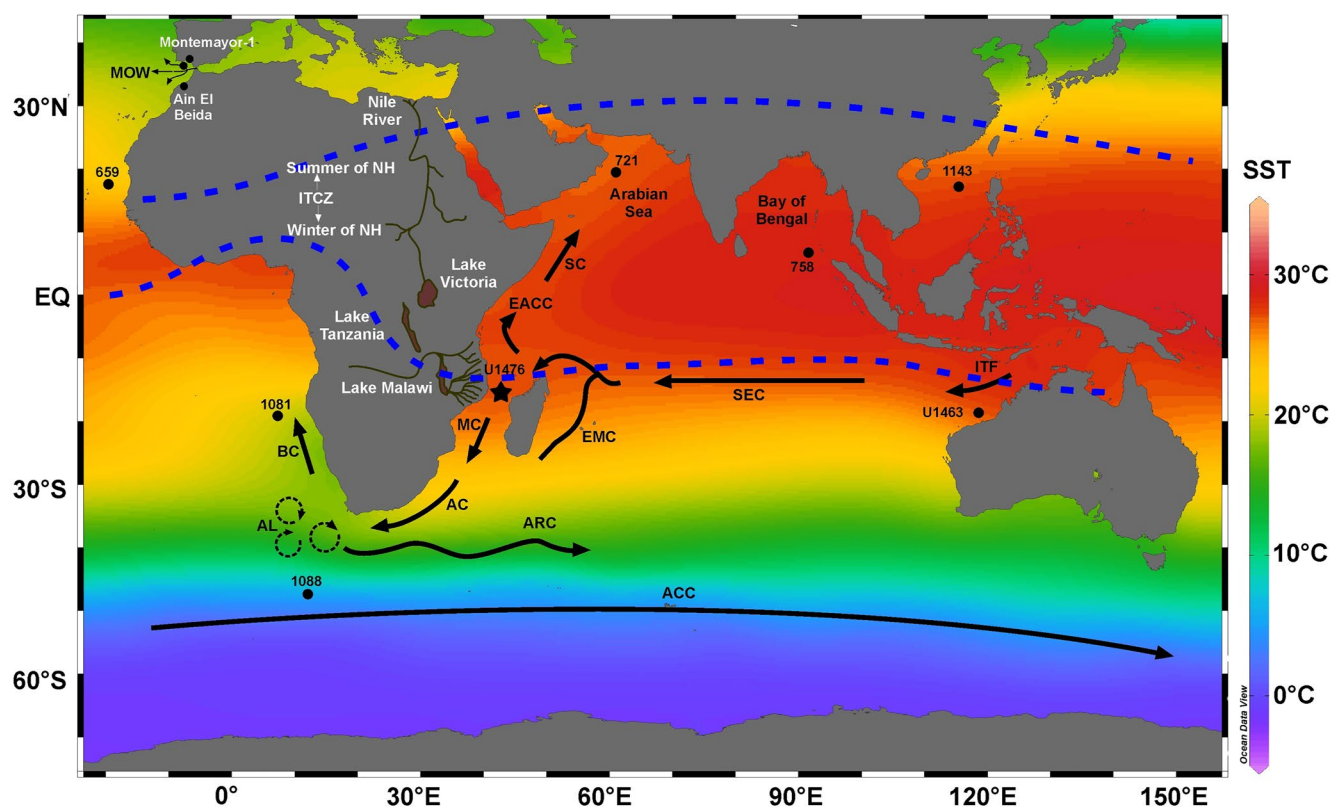


Figure 1. Location map of the present study, Site U1476 (black star, entrance of Mozambique Channel) and mentioned sites in the discussion from the Atlantic (Ain El Beida section; Krijgsman et al., 2004; Montemayor-1 section, Pérez-Asensio et al., 2013; Montemayor-1 borehole, van der Berg et al., 2015; ODP Site 1081, Hoetzel et al., 2015; ODP Site 659, Colin et al., 2014), Indian (Site 721, Diester-Haass et al., 2006; Site 758, Gupta & Thomas, 2003; Site U1463, Christensen et al., 2017) and Pacific Ocean (Site 1146, Holbourn et al., 2018) over the perspective of modern oceanographic settings (i.e., sea surface temperature, SST). Black arrows indicate the surface water masses. MOW, Mediterranean Outflow Water; ITF, Indonesian Throughflow; SEC, South Equatorial Current; NEMC, North Equatorial Madagascar Current; EMC, East Madagascar Current; MC, Mozambique Current; AC, Agulhas Current; EACC, East African Coastal Current; SC, Somalia Current; ARC, Agulhas Retroflection Current; BC, Benguela Current; AL, Agulhas Leakage; ACC, Antarctic Circumpolar Current. Dashed blue lines represent the ITCZ position during the summer and winter of northern hemisphere.

a north-south pressure gradient which allows a strengthened moisture flux over southern Africa (DeBlander & Shaman, 2017; Xulu et al., 2020). These seasonal shifts of ITCZ bring heavy rains through SAFM (most southward position of ITCZ) (Clark et al., 2003; McClanahan, 1988; Tyson & Preston-Whyte, 2000) influencing the small rivers catchments near the studied site.

Thus, marine sediments from the western Indian Ocean are potentially an ideal archive for monitoring local changes in SAFM as these riverine discharge fluctuations are controlled by monsoon precipitation linked to the ITCZ movement (van der Lubbe et al., 2021).

Oceanographically, the entrance of the Mozambique Channel is influenced by tropical and subtropical surface water masses, which form an intermittent flow that lasts for a short time and is usually referred as to Mozambique Current or Mozambique Channel Throughflow (hereafter MCT, Lutjeharms, 2006). Its origin occurs the within Indian Ocean subtropical gyre, via the westward flow of the South Equatorial Current (SEC), which reaches Madagascar and splits into a northern and southern limb forming the East African Coastal Current (EACC) and the hereafter MCT, respectively (Schott et al., 2009). These waters are warm (~30°C during the summer), stratified year-round, and have low nutrients (McClanahan, 1988). Mesoscale eddies are created per year in this region (Schouten et al., 2003) merging at south of the Mozambique Channel (Ternon et al., 2014), triggering cyclonic perturbations, causing shedding of Agulhas rings south of Africa, and thus controlling interocean salt and heat exchange (Biaostoch et al., 2008). Moreover, they act together with riverine input to enhance zooplankton biomass and to create habitats for higher-trophic animals (Lutjeharms, 2006).

3. Material and Methods

3.1. Elemental Geochemistry and Granulometric Analysis

The elemental intensities of Si, K, Ca, and Ti were measured at high resolution (1 cm) using an Avaatech XRF core scanner at the Scripps Institute of Oceanography (USA). X-ray fluorescence (XRF) data for this study were collected over a 1 cm² area using 30 s count time, and intensity conditions of 10 and 30 kV. After previous cleaning, the surface sediments of core halves were covered with SPEXCerti Ultralene in order to avoid interferences such as drying and contamination. We exhibited the XRF data in the natural log (ln) of relevant elemental ratios, as it provides a more accurate and precise value of sediment composition (Pawłowsky-Glahn & Buccianti, 2011; Weltje & Tjallingii, 2008).

Grain size analyses ($n = 130$) were conducted using a Mastersizer 3000 laser diffraction particle size analyzer (Malvern Instruments Ltd.) equipped with a Hydro LV unit at Niigata University (Japan). The measurement range for grain size analysis was 0.01–2,100 μm . Particles were separated using an ultrasonic dispersion treatment in which samples were placed in a water solution containing 0.2 wt.% sodium hexametaphosphate for 1 min. The refractive index was set to 1.580 and the absorption index was set to 0.100 for red laser. The refractive index was set to 2.000 and the absorption index was set to 0.100 for blue laser. Measurement time was 5 s per sample for both the red and blue lasers and measurements were repeated 5 times. The optimal obscuration for the measurements ranged between 8% and 12%. Clay content (under 3.906 μm) and sand contents (0.062–2,100 mm) were calculated using the Malvern Mastersizer software (version 3.1).

3.2. Cyclostratigraphic, Spectral Analysis, and Sedimentation Rate

The use of spectral analysis in our record is divided in two approaches: the first one was carried out on an untuned ln(Si/K) ratio to help constrain our high-resolution age model, and the second was accomplished on the paleoclimate proxy data placed on the ln(Si/K) tuned age model in order to observe the predominant orbital forcing signals. In the former, we preprocessed evenly spaced data (0.01 m) by detrending it to 36% and applied spectral analysis. In latter, it was detrended by 35% to remove the long-term trend (Cleveland, 1979) by LOWESS smooth curve.

The dominant cycles (peaks) and statistical significance test were observed through multitaper method (MTM) power spectral analysis (Thomson, 1982) and robust red noise modeling procedure (Mann & Lees, 1996), respectively. All peaks above the confidence level of 95% in the spectral analysis were compared to astronomical frequencies from La2004 solution (Laskar et al., 2004). By applying Fast Fourier transform (FFT) (Kodama & Hinnov, 2015), we analyzed the evolution of signal frequencies through geologic time. All cyclostratigraphic and spectral analysis described below were compiled on the Acycle software package (Li et al., 2019).

3.3. Principal Component Analysis (PCA) and Pearson Correlation Coefficient

We performed PCA through the software Paleontological Statistics—PAST (Hammer et al., 2001) and Pearson correlation coefficients on major elements (i.e., Al, Si, K, Ca, Ti, Fe, Br, Rb, Sr, Zr, and Ba) from Site U1476 sediments. We aimed to comprehend the main factor influencing the geochemical composition of sediments gathered in the entrance of Mozambique Channel. The pretreatment applied on the data included normalization, subtraction of mean values, and division by standard deviation (Davis, 1986). Principal components (PCs) with eigenvalues (axis values) of <0.8 were excluded from the interpretation as they do not represent significant influence on records. Pearson correlation coefficients were calculated to identify meaningful relationships among PCs and elements.

3.4. Oxygen and Carbon Isotopes

We measure $\delta^{18}\text{O}$ and $\delta^{13}\text{C}$, on planktonic species *Orbulina universa* ($>150 \mu\text{m}$), which is a hyposaline tolerant species (Bé & Tolderund, 1971). For each one of the 150 samples approximately 10 shells were handpicked under a stereomicroscope. Those ratios were determined through CO_2 obtained offline by reaction with 103% H_3PO_4 (Craig, 1957; McCrea, 1950), measured on a second dual-inlet SIRA-II mass spectrometer, at the Servicio General de Análisis de Isótopos Estables (NUCLEUS, Universidad de Salamanca). The isotope results are

expressed in per mil (‰) and represents deviations from VSMOW (Vienna Standard Mean Ocean Water) for oxygen and PDB (Pee Dee Belemnite) for carbon. Analytical precision was determined by repeated analysis on both internal and international reference materials, consisting in $\pm 0.2\text{‰}$ for $\delta^{18}\text{O}$ and $\pm 0.1\text{‰}$ for $\delta^{13}\text{C}$.

4. Results

4.1. Elemental Geochemistry and Sediment Grain Size

The $\ln(\text{Ca}/\text{Ti})$ and $\ln(\text{Si}/\text{K})$ ratios showed similar trend along the entire record. They exhibit the lowest values at two depth intervals (172–178 and 209–215 m). The sand fraction displays general flat pattern showing small range of variation (0%–2%). Otherwise, the percentual of clays presents a significant gradual drop (black arrow, Figure 2) between ~ 241 and ~ 167 m.

4.2. Oxygen and Carbon Isotope Signal of *O. universa*

All values of $\delta^{18}\text{O}$ values of *O. universa* from U1476 ranges from -0.5‰ to -3‰ . Two smooth enrichments can be observed from 200 to ~ 182 m and from 174 to 165 m. $\delta^{13}\text{C}$ showed high values within a range of 1‰ and $\sim 2.55\text{‰}$ (Figure 2). A remarkable drop observed in $\delta^{13}\text{C}$ values also occurs in $\delta^{18}\text{O}$ values between 172 and 178 mbsf (gray bar, Figure 2).

4.3. Spectral Analysis

The spectral analysis (see Section 3.2) of the untuned $\ln(\text{Si}/\text{K})$ ratio, revealed that higher power frequency was concentrated in two depth intervals (132–171 and 191–242 m) and marked by cycles of 1, 0.8, and 0.6 m above the 95% level of confidence from autoregressive model (Figure 3a). Low power frequency was observed in a range of 170–225 m and they exhibit cycles of 20 and ~ 11 m.

4.4. Statistical Analysis

The PCA of major elements of U1476 sediments exhibits two major PCs that together explain 89.1% of the variance of the XRF records (Table 1). PC 1, explaining 80.6% of the total variance, shows high loadings for Al, Si, K, Ti, Fe, Rb, and to a lesser degree Zr and Ba (Figure 4). The former elements show correlation coefficients higher than 0.95 (Table 2).

5. Discussion

5.1. Age Model and Astronomical Tuning

The age model developed in the present study has precession scale resolution from 7.4 to 4.5 Ma (109.86-m thick, 131.98–241.84 mbsf of U1476 splice, including holes U1476A, U1476D, and U1476E). Previous astronomically dated biostratigraphic data (tie points, Table 3) were used to constrain the age model (Table 4) based on Si/K ratio depths tuned to NH summer insolation. The bottom of *Ceratholithus acutus* has been dated in 5.32–5.35 Ma in different sections in the Atlantic Ocean (Backman et al., 2012; Lourens et al., 2004). This event occurred near the minimum of the long eccentricity cycle spanning between 5.6 and 5.2 Ma (Backman et al., 2012; Lourens et al., 2004). In the same way, the Top occurrence of *Discoaster quinqueringus*, and the top of *Nicklithus amplificus* were recorded at 191 mbsf, and astronomically dated at 5.54–5.59 Ma and 5.94–6 Ma, respectively (Backman et al., 2012; Lourens et al., 2004). The number of short-term cycles recorded in the Si/K ratio between the bottom of *C. acutus* and the bottom of *N. amplificus* assuming a periodicity of 1 cycle every 0.8–1 m fits well with an average length of 22,000 years. According to these preliminary ages we can conclude that the short-term cycles (0.8–1 m) correspond to precession. Based on these initial chronological constraints the record of Si/K was tuned to NH summer insolation, assuming that lower Si/K was related to NH summer insolation minima (see Section 5.3). The cyclical patterns in amplitude of the Si/K ratio were used for the tuning, with special attention to the low amplitude cycles typically associated to low amplitude variations in precession during eccentricity minima, while high amplitude variations in the precession-driven Si/K cycles were related to eccentricity maxima. All the tie points used for the cyclostratigraphic tuning are listed in Table 3. Thus, the studied interval

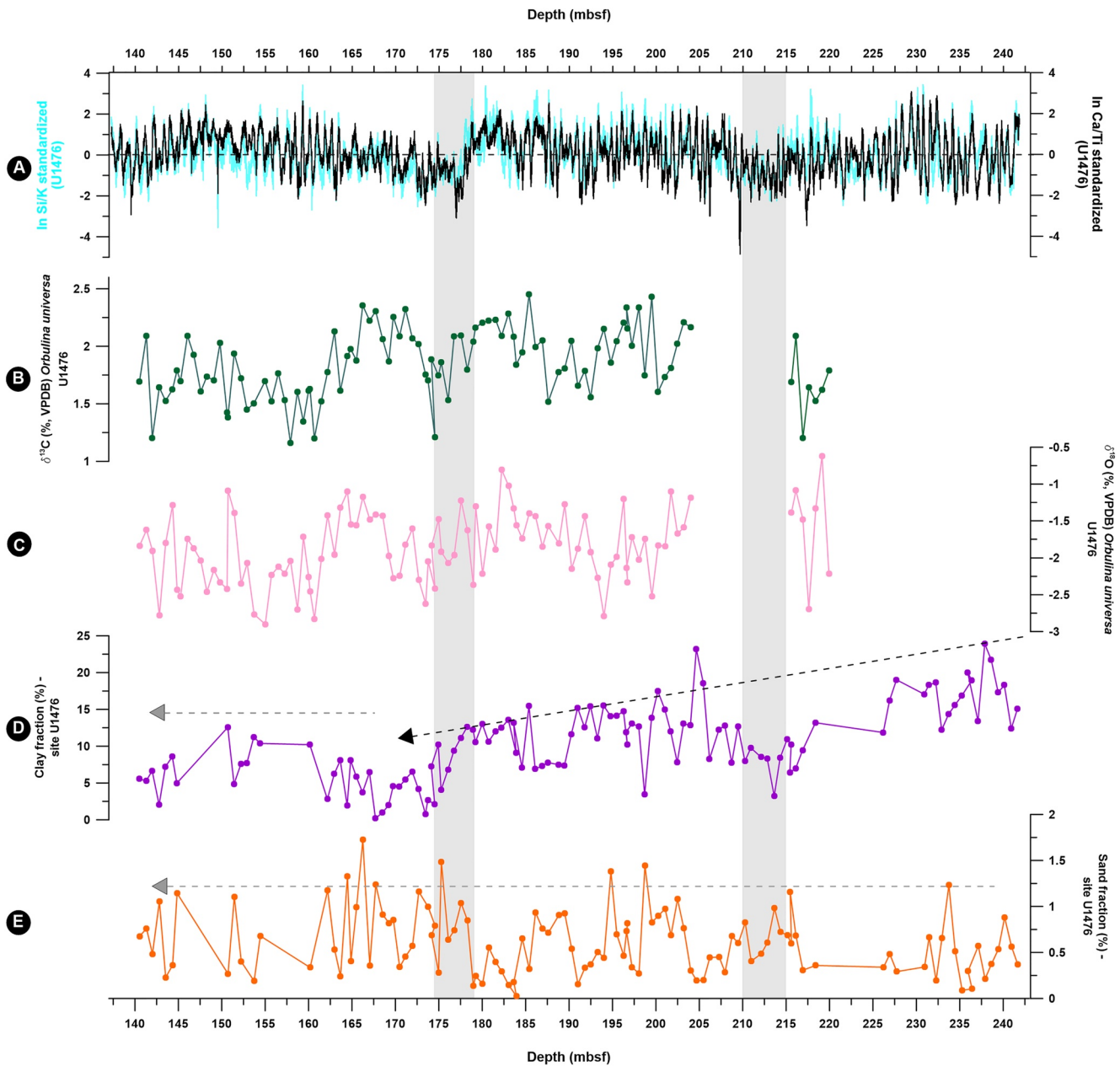


Figure 2. Integrated data of Site U1476 plotted against meter below sea floor (mbsf). (a) Similar trend between standardized $\ln(\text{Si}/\text{K})$ and $\ln(\text{Ca}/\text{Ti})$ ratios. (b) Relatively high values of $\delta^{13}\text{C}$ of planktic foraminifera *Orbulina universa*. (c) Low values of $\delta^{18}\text{O}$ from *O. universa*. (d) Clay fraction exhibited in percentage (%) showing significant drop (black arrow) until ~ 170 mbsf and following flat pattern (horizontal grey arrow). (e) Flat pattern of sand fraction.

of Site U1476 represents a unique continuous sedimentary succession spanning from late Miocene (~ 7.4 Ma) to early Pliocene (~ 4.5 Ma) (Figure 2e), with sedimentation rates varying from ~ 3.5 to 5.5 cm/kyr.

5.2. Interpretation of the Geochemical Cycles

Elemental (Ca/Ti and Si/K ratios) proxies were interpreted together with PCA to comprehend the driving mechanism on SAFM evolution during the late Miocene-early Pliocene transition interval. The Ca/Ti ratio measures the relative proportion of biogenic calcite (Ca) versus terrigenous matter (Ti) in the sediment and has been often related to changes in biological productivity (Ca) versus detrital input (Ti) (Burone et al., 2019; Izumi et al., 2021; Maiorano et al., 2015; Riethdorf et al., 2013). Therefore, this proxy may reflect changes in productivity or varia-

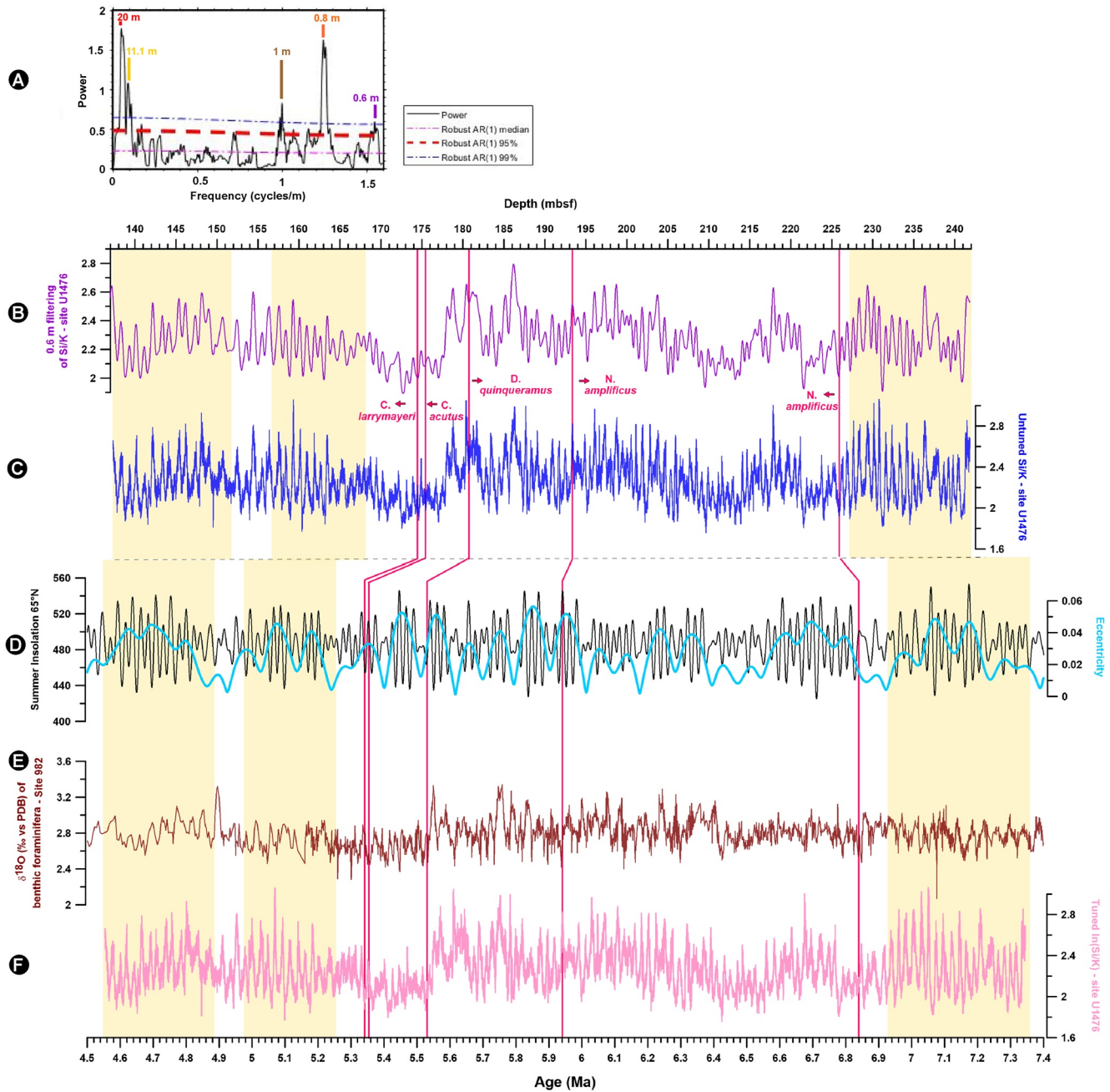


Figure 3. Age model of Site U1476: (a) Spectral analysis carried out on untuned Si/K ratio data showing the most expressive cycles (20–0.6 m) above 95% of confidence level. (b) Purple line is the filtering output of 0.6 m. (c) Si/K ratio untuned records. (d) Summer insolation at 65°N. (e) $\delta^{18}\text{O}$ of benthic foraminifera from Site 982 (Drury et al., 2016). (f) Tuned $\ln(\text{Si}/\text{K})$ ratio. Pink vertical lines represent the biostratigraphic datum of the following index taxa: *Ceratolithus larrymayeri*, *Ceratolithus acutus*, *Discoaster quinqueramus*, and *Nicklithus amplificus*. Light yellow shading indicates the correlation between the untuned Si/K ratio, summer insolation 65°N, eccentricity, $\delta^{18}\text{O}$ values from Site 982, and filtering output.

tions in detrital input to the basin or both. The results of PCA from U1476 elements indicate that $\ln(\text{Ca}/\text{Ti})$ ratio also agree with this previous interpretation. Ca and Ti exhibits opposite loadings (Figure 4) and are coherent with a carbonate-based productivity versus detrital input depositional setting. In sites where productivity is almost constant during glacial interglacial cycle, $\ln(\text{Ca}/\text{Ti})$ ratio variations mainly correspond to detrital input, with minima in $\ln(\text{Ca}/\text{Ti})$ ratio corresponding to high riverine input (Ardi et al., 2020; Courtillot et al., 2020; Jaeschke et al., 2007).

Table 1
Principal Components of Site U1476 From 135.014 to 241.840 m

PC	Eigenvalue	Variance (%)
1	8.06	80.63
2	0.85	8.51
3	0.54	5.37

To better understand which of the two mechanisms is driving the Ca/Ti record, we compared it with the Si/K ratio which has been attributed to riverine input (Joussain et al., 2016; Sun et al., 2016). Si associated to quartz and coarser siliciclastics (Rodríguez-López et al., 2006) and K to the alumino-silicates (clays; Zarriess & Mackensen, 2010; Zarriess et al., 2011). Minima in ln(Si/K) ratio can correspond to the enhancements of winter monsoon precipitation in the southern hemisphere during glacial periods (Wehausen & Brumsack, 2002). The comparison of ln(Ca/Ti) and ln(Si/K) ratio throughout the entire U1476 record displays consistent similarity, which

is corroborated by high r^2 value of 0.78 (Table 2). The difference between both can likely be associated with the variations in carbonate productivity or to changes in chemical weathering processes as K is more mobile than Si (e.g., Lupker et al., 2013), and therefore low Si/K ratio tend to indicate less intense weathering that do not affect ln(Ca/Ti) ratio. In consequence, we relate minima in Si/K ratio and minima in Ca/Ti ratio to maximum detrital input to the Mozambique Channel during the late Miocene-early Pliocene associated to intense rainfall periods inland. Based on this assumption a period of average higher Ca/Ti and higher Si/K, showing lower rainfall in South of Africa was recognized between 6.4 and 5.55 Ma, preceded and followed by two periods of higher detrital supply to the Mozambique Channel, the first one centered at around 6.5 Ma and the second near 5.4 Ma. This long-term oscillation generates the long-term cycle of ~20 m seen in the spectral analysis in the depth domain (see Section 5.4 and Figure 3a).

5.3. Phase Relationship Between Si/K Sedimentary Cycles and Precession

Sediment color reflectance in U1476 changed as a function of the carbonate content, with higher reflectance, whiter colors, indicating higher values of Ca and therefore higher Ca/Ti (Hall et al., 2017). During the last kyr, especially in the early Holocene, 11 kyr ago, at the time of maximum summer insolation in the northern hemisphere, during formation of sapropel 1 in the eastern Mediterranean due to northward shift of the ITCZ and maximum intensification of north African summer monsoon, rainfall in southern Africa was minimum, as demonstrated by the higher values of ln(Ca/Ti). In contrast, today, with minimum summer insolation in the northern hemisphere, ln(Ca/Ti) is minimum, indicating maximum precipitation in southern Africa driven by a southward shift of the ITCZ, which was probably caused by an intensification of winter monsoons in the northern hemisphere. The strong similarity between northern hemisphere summer insolation and the ln(Ca/Ti)

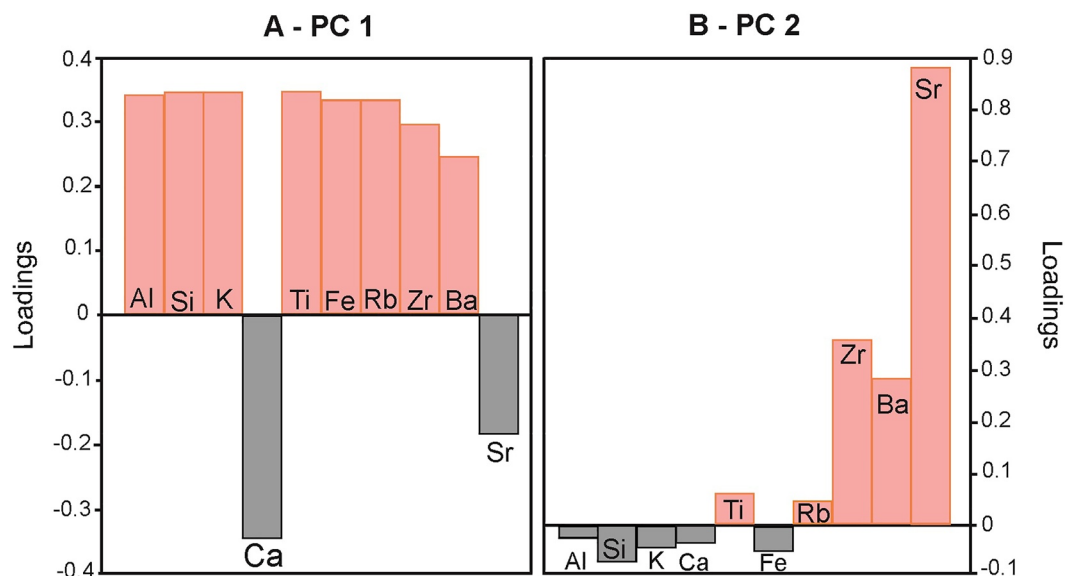


Figure 4. Loadings values of two major principal components of U1476 sediments: (a) PC 1 indicates the dominance of continental sediments. (b) PC 2 is dominated by Sr and Zr.

Table 2
Pearson Correlation Coefficient of the Major Principal Component (PC 1) of Site U1476 and Studied Elements

Elements	PC 1
Al	0.97
Si	0.98
K	0.98
Ca	−0.99
Ti	0.98
Fe	0.95
Rb	0.95
Zr	0.84
Ba	0.70
Sr	−0.52

Note. Bold values represent highest positive correlation coefficients.

demonstrates the link between both parameters (Figure 5). In consequence, we related minimum Ca/Ti with minimum summer insolation in the northern hemisphere.

5.4. Orbital Time Scale Variations of SAFM From Late Miocene to Early Pliocene

The spectral analysis of ln(Si/K) ratio revealed the predominance of four different settings of orbital forcing from late Miocene to early Pliocene. First, precessional cycles (23.8 kyr) drove SAFM variability from 7.4 to ~6.9 Ma (Figure 6d). At 6.9 Ma a marked shift of power toward low frequency cycles occurred (405-kyr long eccentricity), this is contemporaneous to a marked increase in global ice volume (Billups, 2002). At ~5.9 Ma, the power of high frequency cycles decreases in our record until 5.3 Ma (Figure 6d) and variability is dominated by long eccentricity. In the early Pliocene, from 5.3 to 4.5 Ma precessional cycles (23.8, 22.7, and 19.2 kyr) again drive SAFM while long eccentricity weakens.

5.4.1. Precessional Pacing of SAFM During Latest Tortonian and Early Messinian

Spectral analysis of the ln(Si/K) ratio from U1476 sediments reveals that orbital precession is the prevailing driver of variability (Figures 6c and 6d) from 7.4 to 6.9 Ma, similar to model simulations (Bosmans et al., 2015; Marzocchi et al., 2015, 2019; Rohling et al., 2015) and other paleoclimate records such as Cretan sedimentary cycles (Krijgsman et al., 1994). Precession-dominated fluctuations in monsoonal activity in low-latitude regions are well documented (Huang et al., 2018; Liu et al., 2014; Xinzhou et al., 2017). These cycles are driven by oscillations of summer insolation in the northern hemisphere (Berger & Loutre, 1997; Milankovitch, 1941; Ruddiman, 2001), resulting in the deposition of sapropels (organic rich beds) during periods of more northward position of ITCZ and intensification of the northern African monsoon, resulting in high freshwater discharge to the Mediterranean (Wagner et al., 2019). Precipitation in tropical Africa, north of the Equator shows an opposite trend compared with our studied record. Intense SAFM system during northern hemisphere insolation minimum will increase fluvial input associated to higher detrital input, as demonstrated by low ln(Ca/Ti) ratio (Figures 7a and 7b). During this period, humid conditions have also been recognized in southwestern Africa, and pollen data from Namibia coast (Site 1081; Hoetzel et al., 2015) that could indicate a southward extension of the SAFM system compared to present days. Thus, during warm conditions with less ice sheet extent, the monsoon belt would move further north and southward.

During at least the last 2 Ma to the present, hydroclimate in southeastern Africa (20–25°S) is controlled by interplay between low-latitude insolation forcing (precession and eccentricity) and changes in ice volume at high latitudes (Caley et al., 2018). Precession drivers of late Miocene SAFM sedimentary records must affect orbital-scale precipitation changes in southeastern Africa and are more closely related to the contrast between land and ocean temperatures than to SST changes. At Site U1476, the ln(Ca/Ti) record suggests that strong SAFM

Table 3
Tie Points Utilized on Age Model Construction of the IODP Site U1476 for the Late Miocene-Early Pliocene

Depth (mbsf)	Tie point	Type	Astronomically calibrated age (Ma)	Reference
171.163	B— <i>Ceratolithus larrymayeri</i>	Bioevent	5.34	Grandstein et al. (2012)
171.963	B— <i>Ceratolithus acutus</i>	Bioevent	5.35	Grandstein et al. (2012)
177.977	T— <i>Discoaster quinqueramus</i>	Bioevent	5.53	Backman et al. (2012)
191.01	T— <i>Nicklithus amplificus</i>	Bioevent	5.94	Grandstein et al. (2012)
239.44	B— <i>Nicklithus amplificus</i>	Bioevent	6.82	Backman et al. (2012)

Note. Depths are exhibited in meters below sea floor (mbsf). T, top or terminal occurrence; B, base occurrence.

Table 4

Age Model for IODP Site U1476 for Late Miocene (7.4 Ma) to Early Pliocene (4.5 Ma) Based on Si/K Ratio Depths Tuned to NH Summer Insolation, and Constrained by Previous Astronomically Dated Biostratigraphic Data

Depth (mbsf)	Age (kyr)
137.27	4,554
148.13	4,802
149.05	4,837
154.45	4,955
159.29	5,070
163.42	5,184
165.27	5,237
167.12	5,274
172.12	5,402
183.39	5,689
187.67	5,784
190.05	5,846
190.5	5,864
193.28	5,940
194.87	5,992
196.09	6,033
197.24	6,069
200.03	6,145
201.12	6,183
205.08	6,286
206.16	6,331
209.15	6,411
209.87	6,433
211.58	6,488
214.1	6,561
214.88	6,596
216.6	6,647
217.85	6,677
218.67	6,697
221.48	6,779
224.01	6,857
225.26	6,886
226.27	6,918
226.86	6,940
228.35	6,983
229.31	7,005
230.14	7,032
230.78	7,053
234.85	7,167
235.58	7,192
236.35	7,210

(intense riverine input) consistently occurs during precession maxima after ~6.9 Ma with this relationship poorly expressed before.

5.4.2. Long Eccentricity Modulation From ~6.9 to ~5.9 Ma

At ~6.9 Ma cyclicity at Site U1476, though still paced by precession, shifted to longer-term frequencies (~405 kyr, Figures 6c and 6d). This shift of power frequency recorded by our data agrees with the increase in global ice volume registered at ~6.9 Ma, based on the increase in $\delta^{18}\text{O}$ values of benthic foraminifera in northeastern Atlantic (Drury et al., 2016; Hodell et al., 2001), Equatorial Pacific (Drury et al., 2017, 2018) and Indian Ocean (Boulton et al., 2022). This increase corresponds to ~40 m of sea level fall (Miller et al., 2020). The aforementioned global cooling was also felt in North Atlantic and Equatorial Pacific (Drury et al., 2016), and north sector of Indian Ocean (Herbert et al., 2016) exhibiting a significant drop.

The dominance of low frequency cyclicity (405 kyr) observed in our data from 6.9 to ~5.9 Ma is also recorded by monsoonal records of eastern Asian region (Ao et al., 2021; Berger & Loutre, 1997; Tabor et al., 2018). In the northern hemisphere, eccentricity maximum (minimum) will strengthen (weaken) the monsoons (Wang, 2019). Our sediments started to be sensitive to long eccentricity since 6.9 Ma, when a northward movement of the Southern Ocean frontal system, as registered by planktonic $\delta^{18}\text{O}$ data from South Atlantic (Site 1088, Tanner et al., 2020). This movement of the frontal system has been related to the Antarctic ice sheet expansion (Grützner et al., 2005). The movement of the frontal system can be accompanied by atmospheric circulation changes, pushing the westerlies northward. This could allow the establishment of a high-pressure cell over South Africa (Dedekind et al., 2016), which pushed ITCZ and Mascarene High northward (Xulu et al., 2020) during the cold intervals as demonstrated by weak SAFM and less riverine input (Figures 7a, 7b, and 8). The relatively cold SSTs from Indian Ocean (Herbert et al., 2016) give clues of the decreasing moisture supply to the continent (due to weakening of easterlies). These long eccentricity cycles can be related to the changes in the dynamics of the carbon cycle when intensification of winter monsoon took place associated to global cooling around 7 Ma (Holbourn et al., 2018). Obtained $\delta^{13}\text{C}$ signal from *O. universa* seems to be registering these long eccentricity cycles (Figure 7d) but also could be linked with internal system oscillations like CO_2 changes (Stap et al., 2020).

5.4.3. Cyclicity During the Latest Miocene and Earliest Pliocene (5.9-5.3 Ma)

From ~5.9 Ma, we observe a weakening in the precessional expression. This weakened precession in our records could be explained by (a) a change in sedimentation rates (Gorgas & Wilkens, 2002), (b) increased bioturbation, and (c) more influence of ice volume. We did not detect significant changes in sedimentation rates so we can discard this factor affecting the capacity of our record to discern high frequency orbital shifts (Figures 6b and 6d). Records with low sedimentation rates, such as U1476 sediments, can be potentially affected by biological disturbance masking high frequency orbital signal (Orme et al., 2015; Su et al., 2019), but to date no significant changes in bioturbation has been observed in our core in the depth which correspond to the discussed period (Hall et al., 2017). During the Messinian glacial period, the ice volume was controlled by obliquity cycles rather than precession as shown in the benthic $\delta^{18}\text{O}$ record (Drury et al., 2018) as

Table 4
Continued

Depth (mbsf)	Age (kyr)
238.64	7,263
239.21	7,283
239.76	7,301
240.53	7,321
241.65	7,342

may be seen in Figure 10b. This intensification in the impact of obliquity over ice volume can mask the expression of precession in the U1476 sedimentary record. Additionally, the increase aridity provided by global ice volume rise followed by internal positive feedback as intensification of dust flux of Sahara desert since ~6.9 Ma (Crocker et al., 2022) and the Tethys Sea shrinkage (Zhang et al., 2014) could have played a major role in orbital forcing sensitivity of this SAFM record. Enhanced aridity in northern hemisphere (i.e., Asian and northern Africa), evidenced by grasses in China (Lu et al., 2020; Wang et al., 2019) and temperature gradients, changed the land-sea heat distribution, promoting atmospheric circulation reorganization and, thus, affecting more intensely the SAFM sensibility to the beat of long-term pacing from 5.9 to ~5.3 Ma.

5.4.4. Early Pliocene Cyclicity

The Miocene-Pliocene Boundary (~5.3 Ma) is well marked in our spectral records and exhibits the resumption of low-latitude forcing expressed by higher frequency cycles modulation (23.8 kyr), consistent with the response of the East Asian monsoon system (Wang et al., 2019). This orbital shift can be attributed to a warmer Earth whose global ice volume declined after 5.5 Ma (Ao et al., 2021). The return of climate system to an interglacial condition (Clotten et al., 2019; Fedorov et al., 2013; O'Brien et al., 2014; Salzmann et al., 2011) associated to sea level changes might have acted as a low filter pass, favoring the tropical forcing instead of high latitude forcing controlled by ice sheet growth. The orbital forcing of SAFM records during the early Pliocene (5.3-4.5 Ma) is quite similar to the interval from 7.4 to 6.9 Ma (Figure 6d) which intense SAFM were linked to maximum precession.

Climate modeling indicate that diminished SST gradient along the equator is linked to a Hadley cell weakening making its southern branch weaker than the northern branch (Briely et al., 2009). Relatively high smectite/kaolinite ratio from the Cape Verde Plateau (ODP Site 659, Colin et al., 2014) implies more humid conditions due the ITCZ influence and monsoon system during early Pliocene. Comparatively, it is likely that the northern limit of ITCZ was similar to its modern position over Africa during the early Pliocene. The weaker southern branch of the Hadley cell influenced the southward position of ITCZ, which did not reach Namibia and favored the aridity in this region (Site 1081, Hoetzel et al., 2015). Low sedimentation rates and low amplitude in $\ln(\text{Ca}/\text{Ti})$ ratio from our study site reinforces the interpretation of critical changes in atmospheric circulation (contraction of rainfall belt in southern hemisphere) during the early Pliocene.

5.5. SAFM and the MSC (5.96-5.33 Ma)

The early restriction of the Atlantic-Mediterranean gateway influence was felt in the Mediterranean Sea since 7.1 Ma, as shown by benthic assemblage related to oxygen deficiency (Bulian et al., 2021; Kouwenhoven et al., 1999) and was more intense at 6.9 Ma (Butler et al., 1995; Roveri et al., 2014; Sierro et al., 2003). Previous studies indicate a link between Mediterranean thermohaline variations during this period and Antarctic evolution associated with a combination of tectonic activity (Capella et al., 2020; Garcia-Castellanos & Villaseñor, 2011) and glacio-eustatic variations induced by orbital forcing (Hodell et al., 1994; Ohneiser et al., 2015), which culminated in the MSC event. At Site U1476, as previously described, we identify a shift toward low power frequency (eccentricity) at ~6.9 Ma linked to an increase in Antarctic Ice Sheet volume.

The dominance of eccentricity forcing recorded in both proxy records from the Mediterranean region at the onset of the MSC (e.g., Hilgen et al., 2007) and the U1476 sediments recording the intensity of SAFM, allows us to suggest a direct climate teleconnection between both regions. Comparison between the $\ln(\text{Ca}/\text{Ti})$ ratio from Montemayor-1 borehole (southwestern Iberian Peninsula; van der Berg et al., 2015) and U1476 reveals similar variability pattern but with probably opposite phase relationship assuming that the relative influence of monsoonal precipitation over these regions between 6.4 Ma and the MSC onset was opposite (Figure 8). In particular, when strong precipitation took place in southern Africa (low $\ln(\text{Ca}/\text{Ti})$ ratio), weak precipitation evidenced by high $\ln(\text{Ca}/\text{Ti})$ ratio were recorded in Montemayor-1 record (Figure 9).

On average between 5.8 and 5.6 Ma climate in southern Iberia was progressively more humid, while in southern Africa, this time is characterized by weak SAFM and a drier climate. During the Messinian glacial period

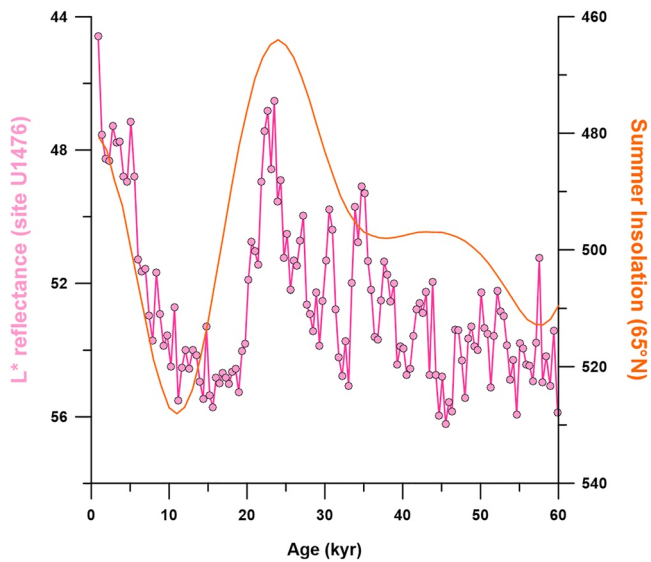


Figure 5. Sedimentological and spectral analysis data of Site U1476 from late Miocene to early Pliocene: (a) Stratigraphic profile composed by foraminifer ooze. (b) Sedimentation rates expressed in cm per kyr (cm/kyr). (c) Spectral analysis exhibiting the peaks above confidence level (95%). (d) Evolutionary spectral analysis and four prevailing orbital forcing from 7.4 to 4.5 Ma. Dashed horizontal black lines marks the shift of power frequencies. Dashed red lines delimits the Messinian Salinity Crisis (MSC).

(~6.4–5.55 Ma, Drury et al., 2016) the main source of moisture associated to the low-latitudes region would have stabilized near the tropical region and for this reason the ITCZ was not reaching the south of Africa neither the influence of midlatitude moisture reached southern Iberia. Persistent high values $\ln(\text{Ca}/\text{Ti})$ and $\ln(\text{Si}/\text{K})$ related to weak SAFM and relatively dry conditions support this interpretation and are also correlated to maximum mean insolation of northern hemisphere. At the MSC acme (~5.55 Ma), we observe the strongest SAFM at Site U1476 activity for the entire MSC and minimum in northern African monsoon (orange bar, Figure 9). Intense riverine input due a more southward ITCZ position is also evidenced by abrupt increasing of potassium (K) content in the north-west shelf of Australia at 5.5 Ma associated to weathering (Site U1463, Christensen et al., 2017). After ~5.5 Ma, the general opposite trend of rainfall in southern Iberia and the SAFM and northern African monsoon is not clear, and the northern African monsoon system seemed to be progressively weakening (Figure 9).

Benthic $\delta^{18}\text{O}$ values reflected global cooling from ~5.4 to ~5.6 Ma (Montemayor-1 borehole, Pérez-Asencio et al., 2013 and planktonic $\delta^{18}\text{O}$ indicated weaken northern African monsoon (Figure 10, Ain el Beida, Krijgsman et al., 2004)). Nevertheless, for studied Site U1476, overall lower Ca/Ti points to an increase in precipitation and SAFM intensification. This is in agreement with models that predicted the MSC weakened the AMOC, which transferred this climate change through the atmosphere favoring a southward shift of ITCZ, cooling of north Africa, and warming of south Africa (Ivanović et al., 2014). Yet, our data support that the MSC affected the atmospheric circulations in a global-scale climate, or at least they occurred synchronously.

5.6. Productivity and Rainfall Intensifications During Miocene-Pliocene Transition

At Site U1476, we observed a persistent long eccentricity cycle in the isotope ($\delta^{13}\text{C}$) records of *O. universa* at least from 6.3 to 5.0 Ma (Figure 7d). At the northwestern Pacific Ocean, similar cyclicality in $\delta^{13}\text{C}$ of planktonic foraminifera between 7.1 and 5.5 Ma, has been associated with the strengthening of winter monsoon during an expansion of ice sheets in the northern hemisphere, affecting marine productivity (Site 1143, Holbourn et al., 2018). In the studied site, the maximum in productivity occurs when the monsoon is weak and is coeval with the most intense paleoproductivity recorded in the west and north Indian Ocean between 6 and 5 Ma (Site 710, Dickens & Owen, 1999; Site 721, Diester-Haass et al., 2006; Site 758, Gupta & Thomas, 2003; Site 707, Hempel & Bohrmann, 1990). The comparison of our isotope data with modern mean $\delta^{13}\text{C}$ value of *O. universa* (0.55‰, Birch et al., 2013) also indicates stronger biological activity during the latest Miocene. These values indicate that our site is also sensitive to the reported late Miocene Biogenic Bloom (LMBB) that has been recognized in many regions and took place between ~8.0 and 4.5 Ma (Drury et al., 2018).

Detrended values of *O. universa* from the Site U1476 $\delta^{18}\text{O}$ can also be interpreted as local fresh water input, salinity, and temperature changes that can be linked to SAFM activity and/or Mozambique Throughflow changes. In near equatorial region, such as Site U1476, temperature variations are small during glacial/interglacial cycles (Herbert et al., 2016; Martinot et al., 2022), so fresh water input and salinity may be the main drivers of the oxygen isotopic record. Detrended and nondetrended *O. universa* $\delta^{18}\text{O}$ values reached a minimum peak at the beginning of the MSC (Figures 7c and 7e) that points to changes in the sea surface conditions. During the latest Miocene and MSC acme we show a general decrease in detrended *O. universa* $\delta^{18}\text{O}$ values (gray bar, Figure 7f) that is compatible with progressive increase in precipitation. Such interpretation is corroborated by a global warming between ~5.5 and 5.3 Ma evidenced by decreasing $\delta^{18}\text{O}$ record of benthic foraminifera (Holbourn et al., 2018; Westerhold et al., 2020).

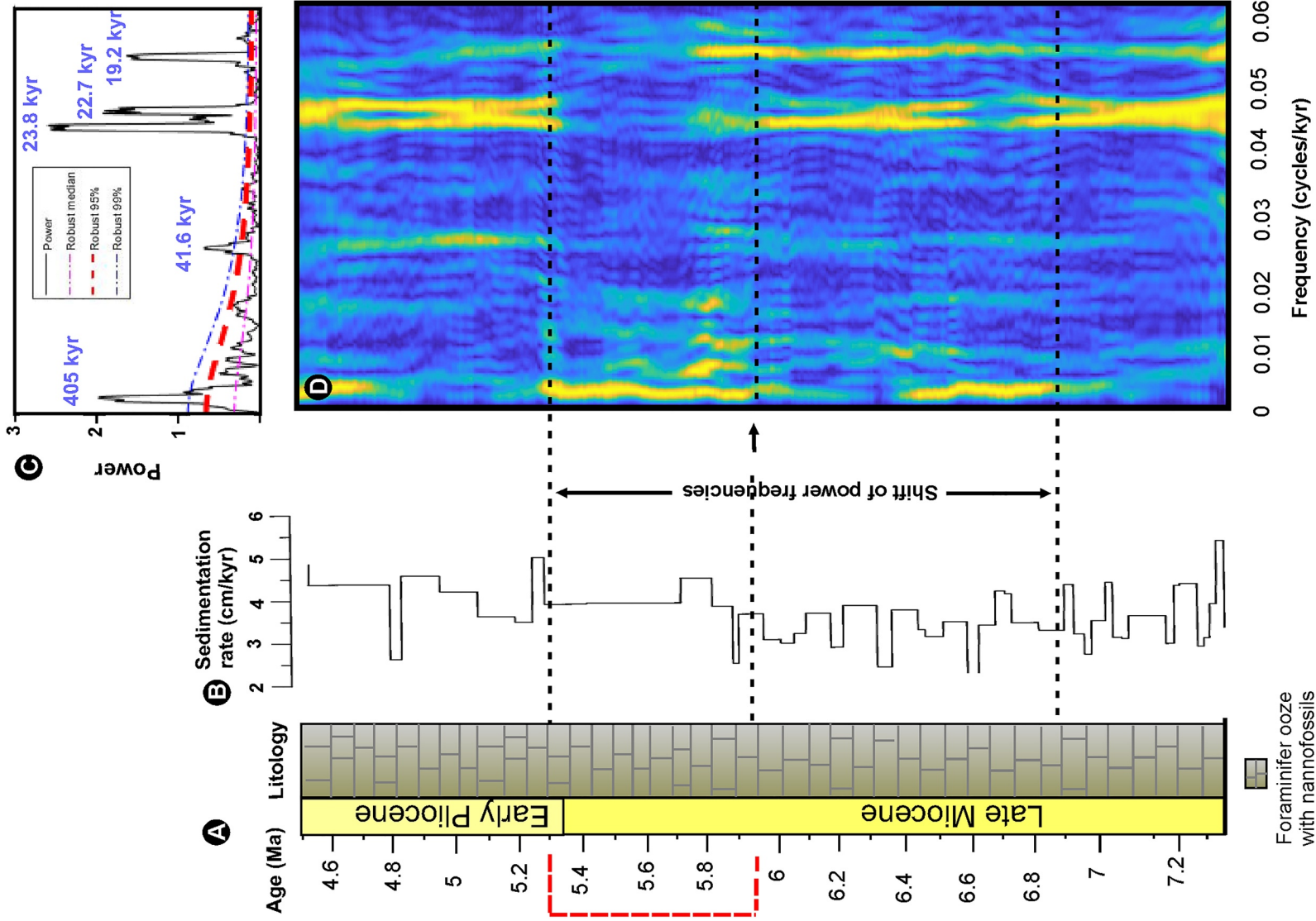


Figure 6. Integrated reflectance from U1476 (age scale from Barker et al. (2022)) and summer insolation (65°N, Laskar et al., 2004) curve exhibiting phase relationship.

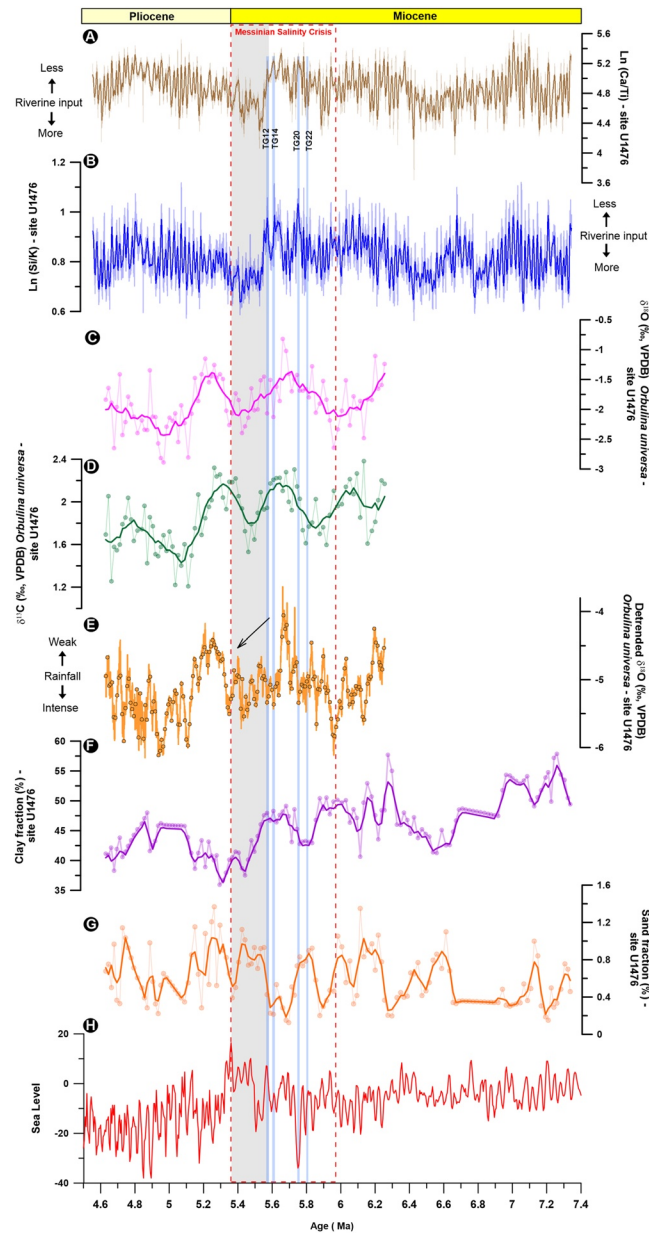


Figure 7. Integrated data of Site U1476 (X-ray fluorescence, grain size, and isotope geochemistry): (a) Ln(Ca/Ti) ratio displaying riverine input versus relative biogenic production. Moving average of 30 points is expressed by dark brown line. (b) Ln(Si/K) ratio reflecting riverine input with moving average of 30 points (dark blue line). (c) $\delta^{18}\text{O}$ values of *O. universa* expressed in permil (‰) calibrated to Vienna Pee Dee belemnite (VPDB) with expressive long-term variability between 5.9 and 5.1 Ma (pink line). (d) Relatively high $\delta^{13}\text{C}$ values *O. universa* and its long-term (400 kyr) variability between 6.2 and ~5.05 Ma (dark green line, moving average of five points). (e) Detrended $\delta^{18}\text{O}$ values of *O. universa* obtained by subtraction of global ice signal. (f) Clay fraction exhibiting decreasing trend (dark purple line, moving average of five points). (g) Sand fraction (moving average of five points highlighted by orange line). Dashed horizontal lines represent the mean values of Ln(Ca/Ti) Ln(Si/K) and $\delta^{18}\text{O}$. (h) Global sea level extracted from benthic foraminifera (Miller et al., 2011). Gray bar and black arrow indicate the intensification of rainfall. Glacial stages TG22, TG20, TG14, and TG12 are represented vertical blue bars.

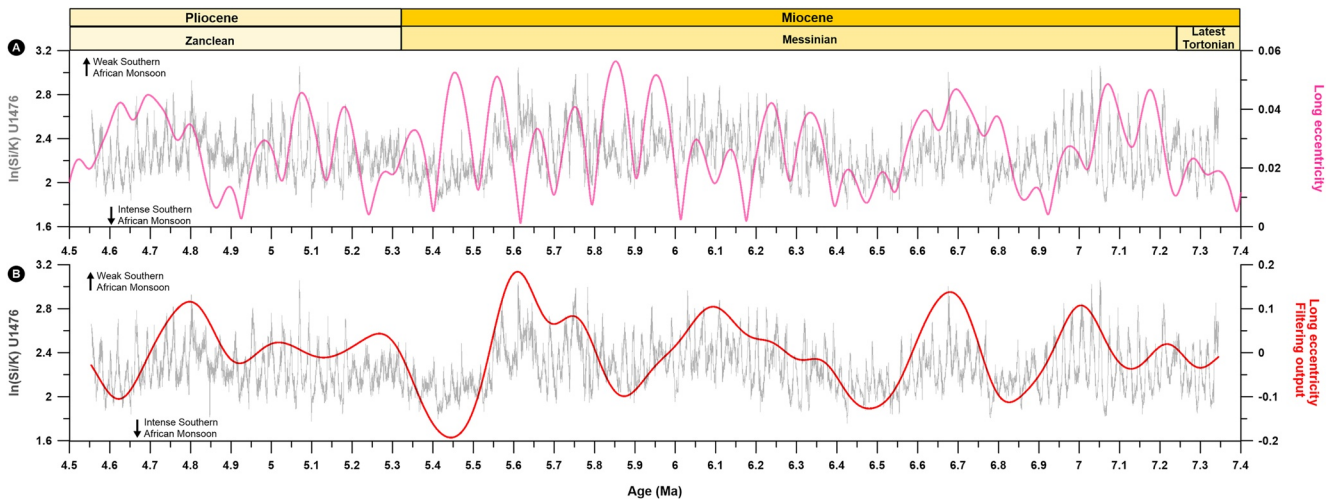


Figure 8. Ln(Si/K) from Site U1476 Ma versus (a) long eccentricity (405 kyr) and (b) Gaussian bandpass filtering from latest Tortonian (~7.4 Ma) to Zanclean (~4.5 ma).

6. Conclusion

We reconstructed the SAFM evolution based on the continuous sedimentary record from IODP Site U1476 (Mozambique Channel) throughout the late Miocene-early Pliocene.

Maximum precession drove intense SAFM from ~7.4 to 6.9 Ma and during the early Pliocene. Eccentricity cycles forced the SAFM contemporaneously to the MSC and synchronous changes have been observed between studied area and Mediterranean Sea dynamic. Orbital forcing influence changes in insolation driving global ice sheet evolution and SSTs that control SAFM.

During the MSC acme at ~5.5 Ma, intense SAFM occurred resulted in enhancement of rainfall in the studied region. Our results agree with models that predict a disruption of the African monsoonal system during the MSC.

Obtained planktonic carbon isotope record is sensitive to the long eccentricity cycle associated with enhancements of the biological pump and monsoon activity and appear to be sensitive to the Late Miocene Biogenic Bloom, observed in other major ocean basins.

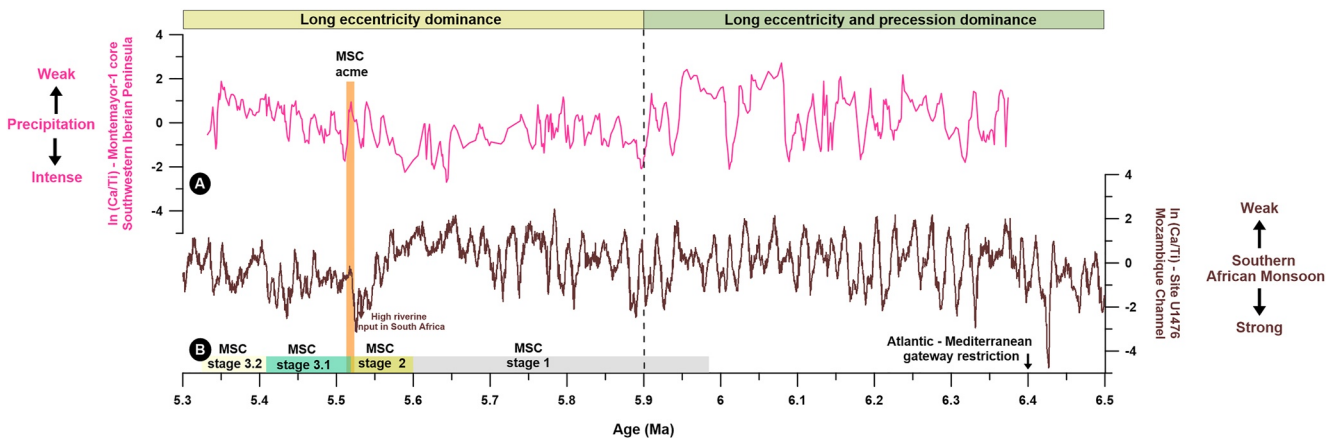


Figure 9. (a) Comparison of riverine input from Site U1476 (our study, brown line) and Montemayor-1 core (van der Berg et al., 2015, pink line). (b) Stages of Messinian Salinity Crisis (MSC, Roveri et al., 2014). Ln(Ca/Ti) values of both sites were standardized in order to make them directly comparable. Orange bar indicates the acme of Messinian Salinity Crisis (~5.5 Ma). Top horizontal bars indicate prevailing orbital forcing. Vertical dashed line highlights the shift of power frequency between two-time intervals.

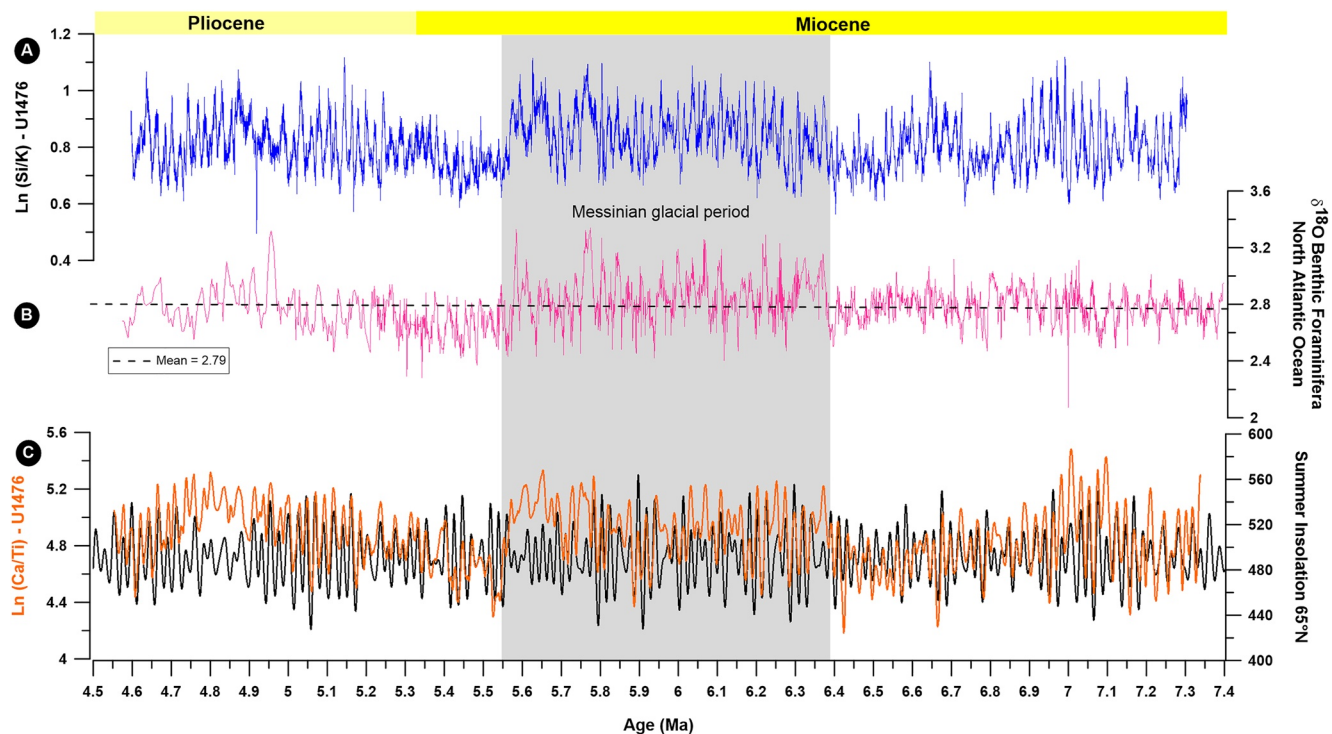


Figure 10. Comparison between Site U1476 data (this study) and global signals from late Miocene to early Pliocene: (a) $\ln(\text{Si}/\text{K})$ ratio from Site U1476. (b) Global ice volume registered in benthic foraminifera from North Atlantic Ocean (Site 982, Drury et al., 2017), (c) $\ln(\text{Ca}/\text{Ti})$ from Site U1476 compared with insolation. Gray bar indicates the Messinian glacial period from ~6.4 to ~5.5 Ma.

Conflict of Interest

The authors declare no conflicts of interest relevant to this study.

Data Availability Statement

All used data from Site U1476 (Ca/Ti , Si/K , $\delta^{18}\text{O}$, $\delta^{13}\text{C}$, and grain size) are available in the PANGAEA database (Azevedo et al., 2023a, 2023b, 2023c). The data of the global sea level are available through Miller et al. (2011). The data of the precipitation pattern (Ca/Ti) from Southwestern Iberia Peninsula are available through van der Berg et al. (2015).

References

- Allen, M. B., & Armstrong, H. A. (2012). Reconciling the intertropical convergence zone, Himalayan/Tibetan tectonics, and the onset of the Asian monsoon system. *Journal of Asian Earth Sciences*, 44, 36–47. <https://doi.org/10.1016/j.jseae.2011.04.018>
- Ao, H., Rohling, E. J., Zhang, R., Roberts, A. P., Holbourn, A. E., Ladant, J.-B., et al. (2021). Global warming-induced Asian hydrological climate transition across the Miocene-Pliocene boundary. *Nature Communications*, 12(1), 6935. <https://doi.org/10.1038/s41467-021-27054-5>
- Ardi, R. D. W., Aswan, K. A. M., Eko, Y., Putra, P. S., Nugroho, S. H., & Istiana (2020). Last Deglaciation-Holocene Australian-Indonesian monsoon rainfall changes off southwest Sumba, Indonesia. *Atmosphere*, 11(9), 932. <https://doi.org/10.3390/atmos11090932>
- Azevedo, A., Jiménez-Espejo, F. J., Bulian, F., Sierro, F. J., Tangunan, D. N., Takashimizu, Y., et al. (2023a). Si/K and Ca/Ti elemental ratios of IODP Site 361-U1476 [Dataset]. PANGAEA. <https://doi.org/10.1594/PANGAEA.961174>
- Azevedo, A., Jiménez-Espejo, F. J., Bulian, F., Sierro, F. J., Tangunan, D. N., Takashimizu, Y., et al. (2023b). Amount of clay and sand from IODP Site 361-U1476 [Dataset]. PANGAEA. <https://doi.org/10.1594/PANGAEA.961176>
- Azevedo, A., Jiménez-Espejo, F. J., Bulian, F., Sierro, F. J., Tangunan, D. N., Takashimizu, Y., et al. (2023c). Stable isotope ratios of *Orbulina universa* from IODP Site 361-U1476 [Dataset]. PANGAEA. <https://doi.org/10.1594/PANGAEA.961175>
- Backman, J., Raffi, I., Rico, D., Fornaciari, E., & Pálfi, H. (2012). Biozonation and biochronology of Miocene through Pleistocene calcareous nannofossils from low and middle latitudes. *Newsletter on Stratigraphy*, 45(3), 221–244. <https://doi.org/10.1127/0078-0421/2012/0022>
- Bahr, A., Kaboth-Bahr, S., & Karas, C. (2023). The opening and closure of oceanic seaways during the Cenozoic: Pacemaker of global climate change? *Geological Society of London*, 523(1), 141–171. <https://doi.org/10.1144/SP523-2021-54>

Acknowledgments

This research used samples provided by the International Ocean Discovery Program (IODP). The authors thank to Editor Dr. Ursula Röhl, Dr. Christian Zeeden, and the anonymous reviewer for improving the quality of our study providing critical review of it. The authors thank to the Operational Oceanography and Paleoclimatology Laboratory (LOOP—Brazil), the Andalusian Earth Sciences Institute (IACT—Spain), the University of Granada (UGR—Spain), and the University of Salamanca (USAL—Spain) for all infrastructure and support. The first author thanks to the Coordenação de Aperfeiçoamento de Pessoal de Nível Superior—CAPES for Ph.D. fellowship (process 88887.372122/2019-00). FJJE and CE has been supported by the Spanish Ministry of Science and Innovation (Grant CTM2017-89711-C2-1-P), cofunded by the European Union through FEDER funds.

- Barker, S., Starr, A., van der Lubbe, J., Doughty, A., Knorr, G., Conn, S., et al. (2022). Persistent influence of precession on northern ice sheet variability since the early Pleistocene. *Science*, 376(6596), 961–967. <https://doi.org/10.1126/science.abm4033>
- Bé, A. W. H., & Tolderund, D. S. (1971). Distribution and ecology of living planktonic foraminifera in surface waters of the Atlantic and Indian Oceans. In B. M. Funnell, & W. R. Riedel (Eds.), *The micropalaeontology of oceans* (pp. 105–149). Cambridge University Press.
- Berger, A., & Loutre, M. F. (1997). Long-term variations in insolation and their effects on climate, the LLN experiments. *Surveys in Geophysics*, 18(2/3), 147–161. <https://doi.org/10.1023/A:1006579708292>
- Biaostoch, A., Böning, C., Lutjeharms, J., & Scheinert, M. (2008). Mesoscale perturbations control inter-ocean exchange south of Africa. *Geophysics Research Letters*, 35, L20602. <https://doi.org/10.1029/2008GL035132>
- Billups, K. (2002). Late Miocene through early Pliocene deep water circulation and climate change viewed from the sub-Antarctic South Atlantic. *Paleogeography, Paleoclimatology, Paleoecology*, 185(3–4), 287–307. [https://doi.org/10.1016/S0031-0182\(02\)00340-1](https://doi.org/10.1016/S0031-0182(02)00340-1)
- Birch, H., Coxall, H. K., Pearson, P. N., Kroon, D., & O'Regan, M. (2013). Planktonic foraminifera stable isotopes and water column structure: Disentangling ecological signals. *Marine Micropaleontology*, 101, 127–145. <https://doi.org/10.1016/j.marmicro.2013.02.002>
- Bolton, C. T., Gray, E., Kuhnt, W., Holbourn, A. E., Lübbert, J., Grant, K., et al. (2022). Secular and orbital-scale variability of equatorial Indian Ocean summer monsoon winds during the late Miocene. *Climate of the Past*, 18(4), 713–738. <https://doi.org/10.5194/cp-18-713-2022>
- Bosmans, J. H. C., Drijfhout, S. S., Tuenter, E., Hilgen, F. J., & Lourens, L. J. (2015). Response of the North African summer monsoon to precession and obliquity forcings in the EC-Earth GCM. *Climate Dynamics*, 44(1–2), 279–297. <https://doi.org/10.1007/s00382-014-2260-z>
- Brierley, C. M., Fedorov, A. V., Liu, Z., Herbert, T. D., Lawrence, K. T., & LaRiviere, J. P. (2009). Greatly expanded tropical warm pool and weakened Hadley circulation in the early Pliocene. *Science*, 323(5922), 1714–1718. <https://doi.org/10.1126/science.1167625>
- Bulian, F., Kouwenhoven, T. J., Jiménez-Espejo, F. J., Krijgsman, W., Andersen, N., & Sierro, F. J. (2021). Impact of the Mediterranean-Atlantic connectivity and the late Miocene carbon shift on deep-sea communities in the western Alboran Basin. *Paleogeography, Paleoclimatology, Paleoecology*, 589, 110841. <https://doi.org/10.1016/j.palaeo.2022.110841>
- Burone, L., Franco-Fraguas, P., De Mahiques, M. M., Lahuerta, N., De Rada, J. R. D., Rodríguez, M., et al. (2019). The Imprint of the geological inheritance and present dynamics on Uruguayan inner shelf sediments (South-Western Atlantic). *Journal of Sedimentary Environments*, 4, 403–420. <https://doi.org/10.12957/jse.2019.47021>
- Butler, R. W. H., Likhorish, W. H., Grasso, M., Pedley, H. M., & Ramberti, L. (1995). Tectonics and sequence stratigraphy in Messinian basins, Sicily: Constraints of the initiation and termination of the Mediterranean salinity crisis. *Bulletin Geological Society of America*, 107, 425–439.
- Caley, T., Extier, T., Collins, J. A., Schefuß, E., Dupont, L., Malaizé, B., et al. (2018). A two-million-year-long hydroclimatic context for hominin evolution in southeastern Africa. *Nature*, 560(7716), 76–79. <https://doi.org/10.1038/s41586-018-0309-6>
- Capella, W., Spakman, W., van Hinsbergen, D. J. J., Chertova, M. V., & Krijgsman, W. (2020). Mantle resistance against Gibraltar slab dragging as a key cause of the Messinian Salinity Crisis. *Terra Nova*, 32(2), 141–150. <https://doi.org/10.1111/ter.12442>
- Carrapa, B., Clementz, M., & Feng, R. (2019). Ecological and hydroclimate responses to strengthening of the Hadley circulation in South America during the late Miocene cooling. *Proceedings of the National Academy of Sciences of the United States of America*, 116(20), 9747–9752. <https://doi.org/10.1073/pnas.1810721116>
- Christensen, B. A., De Vleeschouwer, D., Henderiks, J., Groeneveld, J., Auer, G., Drury, A. J., et al. (2021). Late Miocene onset of Tasman Leakage and southern hemisphere supergyre ushers in near-modern circulation. *Geophysics Research Letters*, 48, e2021GL095036. <https://doi.org/10.1029/2021GL095036>
- Christensen, B. A., Renema, W., Henderiks, J., De Vleeschouwer, D., Groeneveld, J., Castañeda, I. S., et al. (2017). Indonesian through-flow drove Australian climate from humid Pliocene to arid Pleistocene. *Geophysics Research Letters*, 44, 6914–6925. <https://doi.org/10.1002/2017GL072977>
- Clark, C. O., Webster, P. J., & Cole, J. E. (2003). Interdecadal variability of the relationship between the Indian Ocean zonal mode and East African coastal rainfall anomalies. *Journal of Climate*, 16(3), 548–554. [https://doi.org/10.1175/1520-0442\(2003\)016<0548:ivotrb>2.0.co;2](https://doi.org/10.1175/1520-0442(2003)016<0548:ivotrb>2.0.co;2)
- Cleveland, W. S. (1979). Robust locally weighted regression and smoothing scatterplots. *Journal of the American Statistical Association*, 74(368), 829–836. <https://doi.org/10.1080/01621459.1979.10481038>
- Clotten, C., Stein, R., Fahl, K., Schreck, M., Risebrobakken, B., & De Schepper, S. (2019). On the causes of Arctic Sea ice in the warm early Pliocene. *Scientific Reports*, 9(1), 989. <https://doi.org/10.1038/s41598-018-37047-y>
- Colin, C., Siani, G., Liu, Z., Blamart, D., Skonieczny, C., Zhao, Y., et al. (2014). Late Miocene to early Pliocene climate variability off NW Africa (ODP Site 659). *Paleogeography, Paleoclimatology, Paleoecology*, 401, 81–95. <https://doi.org/10.1016/j.palaeo.2014.02.015>
- Courtillot, M., Hallenberger, M., Bassetti, M.-A., Aubert, D., Jeandel, C., Reuning, L., et al. (2020). New record of dust input and provenance during glacial periods in western Australia shelf (IODP Expedition 356, Site U1461) from the middle to late Pleistocene. *Atmosphere*, 11, 1251. <https://doi.org/10.3390/atmos11111251>
- Craig, H. (1957). Isotopic standards for carbon and oxygen and correction factors for mass-spectrometric analysis of carbon dioxide. *Geochimica et Cosmochimica Acta*, 12(1–2), 133–149. [https://doi.org/10.1016/0016-7037\(57\)90024-8](https://doi.org/10.1016/0016-7037(57)90024-8)
- Crocker, A. J., Naafs, B. D. A., Westerhold, T., James, R. H., Cooper, M. J., Röhl, U., et al. (2022). Astronomically controlled aridity in the Sahara since at least 11 million years ago. *Nature Geoscience*, 15(8), 671–676. <https://doi.org/10.1038/s41561-022-00990-7>
- Davis, J. C. (1986). *Statistics and data analysis in geology* (3rd ed.). Wiley.
- DeBlander, E., & Shaman, J. (2017). Teleconnection between the South Atlantic convergence zone and the southern Indian ocean: Implications for tropical cyclone activity. *Journal of Geophysical Research: Atmospheres*, 122, 728–740. <https://doi.org/10.1002/2016JD025373>
- Dedekind, Z., Engelbrecht, F. A., & van der Merwe, J. (2016). Model simulations of rainfall over southern Africa and its eastern escarpment. *Water SA*, 42(1), 129–143. <https://doi.org/10.4314/wsa.v42i1.13>
- de Oliveira, C. P., Aímola, L., Ambrizzi, T., & Freitas, A. C. V. (2018). The influence of the regional Hadley and Walker circulations on precipitation patterns over Africa in El Niño, La Niña, and neutral years. *Pure and Applied Geophysics*, 175, 2293–2306. <https://doi.org/10.1007/s00024-018-1782-4>
- Dickens, G. R., & Owen, R. M. (1999). The latest Miocene-early Pliocene biogenic bloom: A revised Indian ocean perspective. *Marine Geology*, 161(1), 75–91. [https://doi.org/10.1016/S0025-3227\(99\)00057-2](https://doi.org/10.1016/S0025-3227(99)00057-2)
- Diester-Haass, L., Billups, K., & Emeis, K. C. (2006). Late Miocene carbon isotope records and marine biological productivity: Was there a (dusty) link? *Paleoceanography*, 21, PA4216. <https://doi.org/10.1029/2006PA001267>
- Drury, A. J., John, C. M., & Shevenell, A. E. (2016). Evaluating climatic response to external radiative forcing during the late Miocene to early Pliocene: New perspectives from eastern equatorial Pacific (IODP U1338) and North Atlantic (ODP 982) locations. *Paleoceanography and Paleoclimatology*, 31, 167–184. <https://doi.org/10.1002/2015PA002881>
- Drury, A. J., Lee, G. P., Gray, W. R., Lyle, M., Westerhold, T., Shevenell, A. E., & John, C. M. (2018). Deciphering the state of the late Miocene to early Pliocene equatorial Pacific. *Paleoceanography and Paleoclimatology*, 33, 246–263. <https://doi.org/10.1002/2017PA003245>

- Drury, A. J., Westerhold, T., Frederichs, F., Tian, J., Wilkens, R., Channele, J. E. T., et al. (2017). Late Miocene climate and time scale reconciliation: Accurate orbital calibration from a deep-sea perspective. *Earth and Planetary Science Letters*, 475, 254–266. <https://doi.org/10.1016/j.epsl.2017.07.038>
- Duggen, S., Hoernle, K., van den Bogaard, P., & Harris, C. (2004). Magmatic evolution of the Alboran region: The role of subduction in forming the western Mediterranean and causing the Messinian Salinity Crisis. *Earth and Planetary Science Letters*, 218(1–2), 91–108. [https://doi.org/10.1016/S0012-821X\(03\)00632-0](https://doi.org/10.1016/S0012-821X(03)00632-0)
- Duggen, S., Hoernle, K., van den Bogaard, P., Rüpke, L., & Phipps Morgan, J. (2003). Deep roots of the Messinian Salinity Crisis. *Nature*, 422(6932), 602–606. <https://doi.org/10.1038/nature01553>
- Fedorov, A. V., Brierley, C. M., Lawrence, K. T., Liu, Z., Dekens, P. S., & Ravelo, A. C. (2013). Patterns and mechanisms of early Pliocene warmth. *Nature*, 496(7443), 43–49. <https://doi.org/10.1038/nature12003>
- García-Castellanos, D., & Villaseñor, A. (2011). Messinian Salinity Crisis regulated by competing tectonics and erosion at the Gibraltar arc. *Nature*, 480(7377), 359–363. <https://doi.org/10.1038/nature10651>
- Gorgas, T. J., & Wilkens, R. H. (2002). Sedimentation rates off SW Africa since the late Miocene deciphered from spectral analyses of borehole and GRA bulk density profiles: ODP sites 1081–1084. *Marine Geology*, 180(1–4), 29–47. [https://doi.org/10.1016/S0025-3227\(01\)00204-3](https://doi.org/10.1016/S0025-3227(01)00204-3)
- Gradstein, F. M., Ogg, J. G., Schmitz, M. D., & Ogg, G. M. (2012). *The Geologic Time Scale 2012*. Elsevier. <https://doi.org/10.1016/B978-0-444-59425-9.00004-4>
- Griffin, D. L. (2002). Aridity and humidity: Two aspects of the late Miocene climate of North Africa and the Mediterranean. *Palaeogeography, Palaeoclimatology, Palaeoecology*, 182(1–2), 65–91. [https://doi.org/10.1016/S0031-0182\(01\)00453-9](https://doi.org/10.1016/S0031-0182(01)00453-9)
- Groeneveld, J., Henderiks, J., Renema, W., McHugh, C. M., De Vleeschouwer, D., Christensen, B. A., et al. (2017). Australian shelf sediments reveal shifts in Miocene southern hemisphere westerlies. *Science Advances*, 3(5), e1602567. <https://doi.org/10.1126/sciadv.1602567>
- Grützer, J., Hillenbrand, C.-D., & Rebesco, M. (2005). Terrigenous flux and biogenic silica deposition at the Antarctic continental rise during the late Miocene to early Pliocene: Implications for ice sheet stability and sea ice coverage. *Global and Planetary Change*, 45(1–3), 131–149. <https://doi.org/10.1016/j.gloplacha.2004.09.004>
- Gupta, A. K., & Thomas, E. (2003). Initiation of northern hemisphere glaciation and strengthening of the northeast Indian monsoon: Ocean Drilling Program Site 758, eastern equatorial Indian Ocean. *Geology*, 31(1), 47–50. [https://doi.org/10.1130/0091-7613\(2003\)031%3C0047:IONHGA%3E2.0.CO;2](https://doi.org/10.1130/0091-7613(2003)031%3C0047:IONHGA%3E2.0.CO;2)
- Hall, I. R., Hemming, S. R., & LeVay, L. J., & the Expedition 361 Scientists. (2017). South African climates (Agulhas LGM density profile). *Paper presented at Proceedings of the International Ocean Discovery Program* (Vol. 361). International Ocean Discovery Program. <https://doi.org/10.14379/iodp.proc.361.2017>
- Hammer, Ø., Harper, D. A. T., & Ryan, P. D. (2001). PAST: Paleontological statistics software package for education and data analysis. *Palaeontologia Electronica*, 4(1), 9. http://palaeo-electronica.org/2001_1/past/issue1_01.htm
- Hempel, P., & Bohrmann, G. (1990). Carbonate-free sediment components and aspects of silica diagenesis at Sites 707, 709, and 711 (Leg 115, western Indian Ocean). In R. A. Duncan, J. Backmann, L. C. Peterson, et al. (Eds.), *Proceedings of the Ocean Drilling Program, Scientific Results* (Vol. 115, pp. 677–698). Ocean Drilling Program. <https://doi.org/10.2973/odp.proc.sr.115.181.1990>
- Herbert, T. D., Lawrence, K. T., Tzanova, A., Peterson, L. C., Caballero-Gill, R., & Kelly, C. S. (2016). Late Miocene global cooling and the rise of modern ecosystems. *Nature Geoscience*, 9(11), 843–847. <https://doi.org/10.1038/ngeo2813>
- Hilgen, F., Kuiper, K., Krijgsman, W., Snell, E., & van der Laan, E. (2007). Astronomical tuning as the basis for high resolution chronostratigraphy: The intricate history of the Messinian Salinity Crisis. *Stratigraphy*, 4, 231–238.
- Hodell, D. A., Benson, R. H. A., Kent, D. V., Boersma, A., & Bied, K. R.-E. (1994). Magnetostratigraphic, biostratigraphic, and stable isotope stratigraphy of an upper Miocene drill core from the Salé Briqueterie (northwestern Morocco): A high-resolution chronology for the Messinian stage. *Paleoceanography*, 9(6), 835–855. <https://doi.org/10.1029/94PA01838>
- Hodell, D. A., Curtis, J. H., Sierro, F. J., & Raymo, M. E. (2001). Correlation of late Miocene to early Pliocene sequences between the Mediterranean and north Atlantic. *Paleoceanography and Paleoclimatology*, 16(2), 164–178. <https://doi.org/10.1029/1999PA000487>
- Hoetzel, S., Dupont, L. M., & Wefer, G. (2015). Miocene-Pliocene vegetation change in south western Africa (ODP Site 1081, offshore Namibia). *Paleoceanography, Palaeoclimatology, Palaeoecology*, 423, 102–108. <https://doi.org/10.1016/j.palaeo.2015.02.002>
- Holbourn, A. E., Kuhnt, W., Clemens, S. C., Kochhann, K. G. D., Jöhncck, J., Lübbers, J., & Andersen, N. (2018). Late Miocene climate cooling and intensification of southeast Asian winter monsoon. *Nature Communications*, 9(1), 1584. <https://doi.org/10.1038/s41467-018-03950-1>
- Hsü, K. J. (1973). The desiccated deep-basin model for the Messinian events. In C. W. Drooger (Ed.), *Messinian events in the Mediterranean* (pp. 60–67). North-Holland Publishing Co.
- Huang, E., Chen, Y., Schefuß, E., Steinke, S., Liu, J., Tian, J., et al. (2018). Precession and glacial-cycle controls of monsoon precipitation isotope changes over East Asia during the Pleistocene. *Earth and Planetary Science Letters*, 494, 1–11. <https://doi.org/10.1016/j.epsl.2018.04.046>
- IPCC. (2021). Summary for Policymakers. In V. MassonDelmotte, P. Zhai, A. Pirani, S. L. Connors, C. Péan, S. Berger, et al. (Eds.), *Climate change 2021: The physical science basis. Contribution of working Group I to the Sixth Assessment Report of the Intergovernmental Panel on Climate Change*.
- Ivanović, R. F., Valdes, P. J., Flecker, R., & Gutjahr, M. (2014). Modelling global-scale climate impacts of the late Miocene Messinian Salinity Crisis. *Climate of the Past*, 10(2), 607–622. <https://doi.org/10.5194/cp-10-607-2014>
- Izumi, K., Haneda, Y., Suganuma, Y., Okada, M., Kubota, Y., Nishida, N., et al. (2021). Multiproxy sedimentological and geochemical analyses across the lower-middle Pleistocene boundary: Chemostratigraphy and paleoenvironment of the Chiba composite section, central Japan. *Progress in Earth and Planetary Science Letters*, 8(1), 10. <https://doi.org/10.1186/s40645-020-00393-5>
- Jaeschke, A., Rühlemann, C., Arz, H., Heil, G., & Lohmann, G. (2007). Coupling of millennial-scale changes in sea surface temperature and precipitation off northeastern Brazil with high-latitude climate shifts during the last glacial period. *Paleoceanography and Paleoclimatology*, 22, PA4206. <https://doi.org/10.1029/2006PA001391>
- Jöhncck, J., Kuhnt, W., Holbourn, A., & Andersen, N. (2020). Variability of the Indian monsoon in the Andaman sea across the Miocene-Pliocene transition. *Paleoceanography and Paleoclimatology*, 35, e2020PA003923. <https://doi.org/10.1029/2020PA003923>
- Joussain, R., Liu, Z., Colin, C., Duchamp-Alphonse, E., Yu, Z., Moreno, E., et al. (2016). Link between Indian monsoon rainfall and physical erosion in the Himalayan system during the Holocene. *Geochemistry, Geophysics, Geosystems*, 18, 3452–3469. <https://doi.org/10.1002/2016GC006762>
- Kaboth-Bahr, S., Gosling, W. D., Vogelsang, R., Bahr, A., Scerri, E. M. L., Asrat, A., et al. (2021). Paleo-ENSO influence on African environments and early modern humans. *Proceedings of the National Academy of Sciences of the United States of America*, 118(23), e2018277118. <https://doi.org/10.1073/pnas.2018277118>
- Kodama, K. P., & Hinnov, L. (2015). *Rock magnetic cyclostratigraphy* (p. 176). Wiley-Blackwell.

- Kouwenhoven, T. J., Seidenkrantz, M. S., & van der Zwaan, G. J. (1999). Deep-water changes: The near-synchronous disappearance of a group of benthic foraminifera from the late Miocene Mediterranean. *Palaeogeography, Palaeoclimatology, Palaeoecology*, *152*(3–4), 259–281. [https://doi.org/10.1016/s0031-0182\(99\)00065-6](https://doi.org/10.1016/s0031-0182(99)00065-6)
- Krijgsman, W., Gaborardi, S., Hilgen, F. J., Iaccarino, S., de Kaenel, E., & van der Laan, E. (2004). Revised astrochronology for the Ain el Beida section (Atlantic Morocco): No glacio-eustatic control for the onset of the Messinian Salinity Crisis. *Stratigraphy*, *1*(1), 87–101.
- Krijgsman, W., Hilgen, F. J., Langereis, G., & Zachariasse, W. J. (1994). The age of the Tortonian/Messinian boundary. *Earth and Planetary Science Letters*, *121*(3–4), 533–547. [https://doi.org/10.1016/0012-821X\(94\)90089-2](https://doi.org/10.1016/0012-821X(94)90089-2)
- Laskar, J., Robutel, P., Joutel, F., Gastineau, M., Correia, A. C. M., & Levrard, B. (2004). A long-term numerical solution for the insolation quantities of the Earth. *Astronomy and Astrophysics*, *428*(1), 261–285. <https://doi.org/10.1051/0004-6361:20041335>
- Li, M., Hinnov, L., & Kump, L. (2019). Acycle: Time-series analysis software for paleoclimate research and education. *Computers & Geosciences*, *127*, 12–22. <https://doi.org/10.1016/j.cageo.2019.02.011>
- Liu, Z., Wen, X., Brady, E. C., Otto-Bliesner, B., Yu, G., Lu, H., et al. (2014). Chinese cave records and the East Asia summer monsoon. *Quaternary Science Reviews*, *83*, 115–128. <https://doi.org/10.1016/j.quascirev.2013.10.021>
- Lourens, L. J., Hilgen, F. J., Schacleton, N. J., Laskar, J., & Wilson, D. (2004). The Neogene period. In F. Gradstein (Ed.), *A geologic time scale 2004* (pp. 409–440). Cambridge University Press.
- Lu, J., Algeo, T. J., Zhuang, G., Yang, J., Xiao, G., Liu, J., et al. (2020). The early Pliocene global expansion of C4 grasslands: A new organic carbon-isotopic dataset from the north China plain. *Palaeogeography, Palaeoclimatology, Palaeoecology*, *538*, 109454. <https://doi.org/10.1016/j.palaeo.2019.109454>
- Lupker, M., France-Lanord, C., Galy, V., Lavé, J., & Kudrass, H. (2013). Increasing chemical weathering in the Himalayan system since the last glacial maximum. *Earth and Planetary Science Letters*, *365*, 243–252. <https://doi.org/10.1016/j.epsl.2013.01.038>
- Lutjehans, J. R. E. (2006). The ocean environment off southeastern Africa: A review. *South African Journal of Science*, *102*, 419–426.
- Maiorano, P., Marino, M., Balestra, B., Flores, J.-A., Hodell, D. A., & Rodrigues, T. (2015). Coccolithophore variability from the Shackleton site (IODP site U1385) through MIS 16–10. *Global and Planetary Change*, *133*, 35–48. <https://doi.org/10.1016/j.gloplacha.2015.07.009>
- Mann, M. E., & Lees, J. M. (1996). Robust estimation of background noise and signal detection in climatic time series. *Climatic Change*, *33*(3), 409–445. <https://doi.org/10.1007/BF00142586>
- Martinot, C., Bolton, C. T., Sarr, A.-C., Donnadiu, Y., Garcia, M., Gray, E., & Tachikawa, K. (2022). Drivers of late Miocene tropical sea surface cooling: A new perspective from the equatorial Indian ocean. *Paleoceanography and Paleoclimatology*, *37*, e2021PA004407. <https://doi.org/10.1029/2021PA004407>
- Marzocchi, A., Flecker, R., Lunt, D. J., Krijgsman, W., & Hilgen, F. J. (2019). Precessional drivers of late Miocene Mediterranean sedimentary sequences: African summer monsoon and Atlantic winter storm tracks. *Paleoceanography and Paleoclimatology*, *34*, 1980–1994. <https://doi.org/10.1029/2019PA003721>
- Marzocchi, A., Lunt, D. J., Flecker, R., Bradshaw, C. D., Farnsworth, A., & Hilgen, F. J. (2015). Orbital control on late Miocene climate and the north African monsoon: Insight from an ensemble of sub-precessional simulations. *Climate of the Past*, *11*(10), 1271–1295. <https://doi.org/10.5194/cp-11-1271-2015>
- Maslin, M. A., Brierley, C. M., Milner, A. M., Shultz, S., Trauth, M. H., & Wilson, K. E. (2014). East African climate pulses and early human evolution. *Quaternary Science Reviews*, *101*, 1–17. <https://doi.org/10.1016/j.quascirev.2014.06.012>
- McClanahan, T. R. (1988). Seasonality in East Africa's coastal waters. *Marine Ecology Progress Series*, *44*, 191–199. <https://doi.org/10.3354/meps044191>
- McCrea, J. M. (1950). On the isotopic chemistry of carbonates and a paleotemperature scale. *Journal of Chemical Physics*, *18*(6), 849–857. <https://doi.org/10.1063/1.1747785>
- Milankovitch, M. (1941). Kanon der Erdbestrahlungen und seine Anwendung auf das Eiszeitenproblem. Royal Serbian Academy. *Journal of Natural Sciences and Mathematics*, *33*.
- Miller, K. G., Browning, J. V., Schmelz, W. J., Kopp, R. E., Mountain, G. S., & Wright, J. D. (2020). Smoothed Cenozoic sea-level relative to modern from deep-sea geochemical and continental margin records. *Science Advances*, *6*(20), eaaz1346. <https://doi.org/10.1126/sciadv.aaz1346>
- Miller, K. G., Mountain, G. S., Wright, J. D., & Browning, J. V. (2011). A 180-million-year record of sea level and ice volume variations from continental margin and deep-sea isotopic records. *Oceanography*, *24*(2), 40–53. <https://doi.org/10.5670/oceanog.2011.26>
- Mudie, P. J., & Helgason, J. (1983). Palynological evidence for Miocene climate cooling in eastern Iceland about 9.8 Myr ago. *Nature*, *303*(5919), 689–692. <https://doi.org/10.1038/303689a0>
- Murphy, L. N., Kirk-Davidoff, D. B., Mahowald, N., & Otto-Bliesner, B. L. (2009). A numerical study of the climate response to lowered Mediterranean Sea level during the Messinian Salinity Crisis. *Palaeogeography, Palaeoclimatology, Palaeoecology*, *279*(1–2), 41–59. <https://doi.org/10.1016/j.palaeo.2009.04.016>
- Ng, Z. L., Ledesma, S., Sierro, F. J., Duarte, D., Llave, E., Arnáiz, A., et al. (2022). Late Miocene evolution of the eastern Deep Algarve basin: Interaction of bottom currents and gravitational processes in a foredeep setting. *Marine and Petroleum Geology*, *141*, 105695. <https://doi.org/10.1016/j.marpetgeo.2022.105695>
- Nicholson, S. E. (2015). Long-term variability of the East African ‘short rains’ and its links to large-scale factors. *International Journal of Climatology*, *35*(13), 3979–3990. <https://doi.org/10.1002/joc.4259>
- O’Brien, C. L., Foster, G. L., Martínez-Botí, M. A., Abell, R., Rae, J. W. B., & Pancost, R. D. (2014). High sea surface temperatures in tropical warm pools during the Pliocene. *Nature Geoscience*, *7*(8), 606–611. <https://doi.org/10.1038/ngeo2194>
- Ohneiser, C., Florindo, F., Stocchi, P., Roberts, A. P., De Conto, R. M., & Pollard, D. (2015). Antarctic glacio-eustatic contributions to late Miocene Mediterranean desiccation and reflooding. *Nature Communications*, *6*(1), 8765. <https://doi.org/10.1038/ncomms9765>
- Orme, L. C., Reinhardt, L., Jones, R. T., Charman, D. J., Croudace, I., Dawson, A., et al. (2015). Investigating the maximum resolution of μ XRF core scanners: A 1800 year storminess reconstruction from the outer Hebrides, Scotland, UK. *The Holocene*, *26*(2), 235–247. <https://doi.org/10.1177/0959683615596819>
- Pawłowsky-Glahn, V., & Buccianti, A. (2011). Compositional data analysis: Theory and applications. In V. Pawłowsky-Glahn, & A. Buccianti (Eds.), *Chapter 18. Natural laws governing the distribution of the elements in geochemistry: The role of the log-ratio approach* (1st ed.). John Wiley & Sons, Ltd.
- Pérez-Asensio, J. N., Aguirre, J., Jiménez-Moreno, G., Schmiedl, G., & Civis, J. (2013). Glacioeustatic control on the origin and cessation of the Messinian Salinity Crisis. *Global and Planetary Change*, *111*, 1–8. <https://doi.org/10.1016/j.gloplacha.2013.08.008>
- Quan, C., Liu, Y. S., Tang, H., & Utescher, T. (2014). Miocene shift of European atmospheric circulation from trade wind to westerlies. *Scientific Reports*, *4*(1), 5660. <https://doi.org/10.1038/srep05660>

- Riethdorf, J.-R., Nürnberg, D., Max, L., Tiedemann, R., Gorbarenko, S. A., & Malakhov, M. I. (2013). Millennial-scale variability of marine productivity and terrigenous matter supply in the western Bering Sea over the past 180 kyr. *Climate of the Past*, 9(3), 1345–1373. <https://doi.org/10.5194/cp-9-1345-2013>
- Rodríguez-López, J. P., de Boer, P. L., Melendez, N., Soria, A. R., & Pardo, G. (2006). Windblown desert sands in coeval shallow marine deposits: A key for the recognition of coastal ergs in the mid-Cretaceous Iberian Basin, Spain. *Terra Nova*, 18(5), 314–320. <https://doi.org/10.1111/j.1365-3121.2006.00695.x>
- Rogerson, M., Rohling, E. J., Bigg, G. R., & Ramirez, J. (2012). Palaeoceanography of the Atlantic-Mediterranean exchange: Overview and first quantitative assessment of climatic forcing. *Reviews of Geophysics*, 50, RG2003. <https://doi.org/10.1029/2011RG000376>
- Rohling, E. J., Marino, G., & Granta, K. M. (2015). Mediterranean climate and oceanography, and the periodic development of anoxic events (sapropels). *Earth-Science Reviews*, 143, 62–97. <https://doi.org/10.1016/j.earscirev.2015.01.008>
- Roveri, M., Flecker, R., Krijgsman, W., Lofi, J., Lugli, S., Manzi, V., et al. (2014). The Messinian Salinity Crisis: Past and future of a great challenge for marine sciences. *Marine Geology*, 352, 25–58. <https://doi.org/10.1016/j.margeo.2014.02.002>
- Ruddiman, W. F. (2001). *Earth's climate: Past and future* (3rd ed., p. 388). W.H. Freeman.
- Salzmann, U., Williams, M., Haywood, A. M., Johnson, A. L. A., Kender, S., & Zalasiewicz, J. (2011). Climate and environment of a Pliocene warm world. *Palaeogeography, Palaeoclimatology, Palaeoecology*, 309(1–2), 1–8. <https://doi.org/10.1016/j.palaeo.2011.05.044>
- Schneck, R., Micheels, A., & Mosbrugger, V. (2010). Climate modelling sensitivity experiments for the Messinian Salinity Crisis. *Palaeogeography, Palaeoclimatology, Palaeoecology*, 286(3–4), 149–163. <https://doi.org/10.1016/j.palaeo.2009.12.011>
- Schott, F. A., Xie, S.-P., & McCreary, J. P., Jr. (2009). Indian Ocean circulation and climate variability. *Reviews of Geophysics*, 47, RG1002. <https://doi.org/10.1029/2007RG000245>
- Schouten, M. W., de Ruijter, W. P. M., van Leeuwen, P. J., & Ridderinkhof, H. (2003). Eddies and variability in the Mozambique channel. *Deep-Sea Research Part II: Topical Studies in Oceanography*, 50(12–13), 1987–2003. [https://doi.org/10.1016/S0967-0645\(03\)00042-0](https://doi.org/10.1016/S0967-0645(03)00042-0)
- Sierro, F. J., Flores, J. A., Francés, G., Vazquez, A., Utrilla, R., Zamarreño, I., et al. (2003). Orbitally controlled oscillations in planktic communities and cyclic changes in western Mediterranean hydrography during the Messinian. *Palaeogeography, Palaeoclimatology, Palaeoecology*, 190, 289–316. [https://doi.org/10.1016/S0031-0182\(02\)00611-9](https://doi.org/10.1016/S0031-0182(02)00611-9)
- Stap, L. B., Knorr, G., & Lohmann, G. (2020). Anti-phased Miocene ice volume and CO₂ changes by transient Antarctic ice sheet variability. *Paleoceanography and Paleoclimatology*, 35, e2020PA003971. <https://doi.org/10.1029/2020PA003971>
- Steinthorsdottir, M., Coxall, H. K., de Boer, A. M., Huber, M., Barbolini, N., Bradshaw, C. D., et al. (2021). The Miocene: The future of the past. *Paleoceanography and Paleoclimatology*, 36, e2020PA004037. <https://doi.org/10.1029/2020PA004037>
- Su, Q., Nie, J., Luo, Z., Li, M., Heermance, R., & Garzion, C. (2019). Detection of strong precession cycles from the late Pliocene sedimentary records of northeastern Tibetan Plateau. *Geochemistry, Geophysics, Geosystems*, 20, 3901–3912. <https://doi.org/10.1029/2019GC008447>
- Sun, J. M., & Liu, T. S. (2006). The age of the Taklimakan desert. *Science*, 312(5780), 1621. <https://doi.org/10.1126/science.1124616>
- Sun, Y., Liang, L., Bloemendal, J., Li, Y., Wu, F., Yao, Z., & Liu, Y. (2016). High-resolution scanning XRF investigation of Chinese loess and its implications for millennial-scale monsoon variability. *Journal of Quaternary Science*, 31(3), 191–202. <https://doi.org/10.1002/jqs.2856>
- Tabor, C. R., Otto-Bliesner, B. L., Brady, E. C., Nusbaumer, J., Zhu, J., Erb, M. P., et al. (2018). Interpreting precession-driven δ¹⁸O variability in the South Asian monsoon region. *Journal of Geophysical Research: Atmospheres*, 123, 5927–5946. <https://doi.org/10.1029/2018JD028424>
- Tanner, T., Hernández-Almeida, I., Drury, A. J., Guitián, J., & Stoll, H. (2020). Decreasing atmospheric CO₂ during the late Miocene cooling. *Paleoceanography and Paleoclimatology*, 35, e2020PA003925. <https://doi.org/10.1029/2020PA003925>
- Ternon, J. F., Roberts, M. J., Morris, T., Hancke, L., & Backeberg, B. (2014). In situ measured current structures of the eddy field in the Mozambique Channel. *Deep Sea Research Part II: Topical Studies in Oceanography*, 100, 10–26. <https://doi.org/10.1016/j.dsr2.2013.10.013>
- Thomson, D. J. (1982). Spectrum estimation and harmonic analysis. *Proceedings of the Institute of Electrical and Electronics Engineers*, 70(9), 1055–1096. <https://doi.org/10.1109/PROC.1982.12433>
- Tyson, P. D., & Preston-Whyte, R. A. (2000). *Weather and climate of southern Africa* (p. 408). Oxford University Press.
- van der Berg, B. C. J., Sierro, F. J., Hilgen, F. J., Flecker, R., Larrasoña, J. C., Krijgsman, W., et al. (2015). Astronomical tuning for the upper Messinian Spanish Atlantic margin: Disentangling basin evolution, climate cyclicity and MOW. *Global and Planetary Change*, 135, 89–103. <https://doi.org/10.1016/j.gloplacha.2015.10.009>
- van der Lubbe, H. J. L., Hall, I. R., Barker, S., Hemming, S. R., Baars, T. F., Starr, A., et al. (2021). Indo-pacific Walker circulation drove Pleistocene African aridification. *Nature*, 598(7882), 618–636. <https://doi.org/10.1038/s41586-021-03896-3>
- Vidal, L., Bickert, T., Wefer, G., & Röhl, U. (2002). Late Miocene stable isotope stratigraphy of SE Atlantic ODP site 1085: Relation to Messinian events. *Marine Geology*, 180(1–4), 71–85. [https://doi.org/10.1016/S0025-3227\(01\)00206-7](https://doi.org/10.1016/S0025-3227(01)00206-7)
- Wagner, B., Vogel, H., Francke, A., Friedrich, T., Donders, T., Lacey, J. H., et al. (2019). Mediterranean winter rainfall in phase with African monsoons during the past 1.36 million years. *Nature*, 573(7773), 256–260. <https://doi.org/10.1038/s41586-019-1529-0>
- Wang, H., Lu, H., Zhao, L., Zhang, H., Lei, F., & Wang, Y. (2019). Asian monsoon rainfall variation during the Pliocene forced by global temperature change. *Nature Communications*, 10(1), 5272. <https://doi.org/10.1038/s41467-019-13338-4>
- Wehausen, R., & Brumsack, H.-J. (2002). Astronomical forcing of the East Asian monsoon mirrored by the composition of Pliocene south China sea sediments. *Earth and Planetary Science Letters*, 201(3–4), 621–636. [https://doi.org/10.1016/S0012-821X\(02\)00746-X](https://doi.org/10.1016/S0012-821X(02)00746-X)
- Weltje, G. J., & Tjallingii, R. (2008). Calibration of XRF core scanners for quantitative geochemical logging of sediment cores: Theory and application. *Earth and Planetary Science Letters*, 274(3–4), 423–438. <https://doi.org/10.1016/j.epsl.2008.07.054>
- Westerhold, T., Marwan, N., Drury, A. J., Liebrand, D., Agnini, C., Anagnostou, E., et al. (2020). An astronomically dated record of Earth's climate and its predictability over the last 66 million years. *Science*, 369(6509), 1383–1387. <https://doi.org/10.1126/science.aba6853>
- Xinzhou, L., Xiaodong, L., & Hongli, Z. (2017). Transient simulation of the Tibetan Plateau modulated distinct orbital-scale precipitation variation in East and South Asia. *Palaeogeography, Palaeoclimatology, Palaeoecology*, 485, 899–905. <https://doi.org/10.1016/j.palaeo.2017.08.005>
- Xulu, N. G., Chikoore, H., Bopape, M.-J. M., & Nethengwe, N. S. (2020). Climatology of the Mascarene high and its influence on weather and climate over southern Africa. *Climate*, 8(7), 86. <https://doi.org/10.3390/cli8070086>
- Zarriess, M., Johnstone, H., Prange, M., Steph, S., Groeneveld, J., Multiza, S., & Mackensen, A. (2011). Bipolar seesaw in the northeastern tropical Atlantic during Heinrich stadials. *Geophysical Research Letters*, 38, L04706. <https://doi.org/10.1029/2010GL046070>
- Zarriess, M., & Mackensen, A. (2010). The tropical rainbelt and productivity changes off northwest Africa: A 31,000-year high-resolution record. *Marine Micropaleontology*, 76(3–4), 76–91. <https://doi.org/10.1016/j.marmicro.2010.06.001>
- Zhang, Y. G., Pagani, M., Liu, Z., Bohaty, S. M., & De Conto, R. (2013). A 40-million-year history of atmospheric CO₂. *Philosophical Transactions of the Royal Society*, 371(2001), 20130096. <https://doi.org/10.1098/rsta.2013.0096>
- Zhang, Z., Ramstein, G., Schuster, M., Li, C., Contoux, C., & Yan, Q. (2014). Aridification of the Sahara desert caused by Tethys Sea shrinkage during the late Miocene. *Nature*, 513(7518), 401–404. <https://doi.org/10.1038/nature13705>